UCLouvain

École polytechnique de Louvain

Influence of graphene on the mechanical properties of copper thin films

Author: **Aymeric DE VINCK**
Supervisors: **Jean-Pierre RASKIN, Thomas PARDOEN**
Readers: **Hosni IDRISSI, Michaël COULOMBIER**
Academic year 2020–2021
Master [120] in Electro-mechanical Engineering

Remerciements

Le stéréoptype d'un travail de recherche est l'isolement dans un laboratoire. Cette année, j'ai pu découvrir que rien ne se faisait complètement seul, et que la communication avec d'autres chercheurs était primordiale pour avancer. La réalisation de ce mémoire a été possible grâce au concours d'une foule de personnes à qui je voudrais témoigner toute ma gratitude.

Je voudrais dans un premier temps remercier mes promoteurs de mémoire, M. Raskin et M. Pardoen, professeurs à l'Ecole polytechnique Louvain (EPL) pour leur optimisme, leur disponibilité et leurs conseils judicieux, qui ont contribué à alimenter ma réflexion.

Je remercie également toute l'équipe des salles propres Winfab d'avoir toujours été présente pour résoudre tous les petits problèmes liés à l'utilisation des machines. Plus particulièrement, Monsieur Michael Coulombier qui était toujours présent pour répondre à mes questions, pour me conseiller et pour m'aider à interpréter certains résultats.

Un immense merci aussi à Mademoiselle Farzaneh Bahrami et Mademoiselle Sahar Jadi pour les heures passées en laboratoire à travailler sur le procédé de fabrication des lab on chips pour cuivre et graphène. Je les remercie pour les nombreux échantillons qu'elles m'ont fourni et qui ont mené aux résultats présentés dans ce mémoire.

Je tiens à remercier Monsieur Wasil Malik pour les innombrables feuilles de graphène de haute qualité qu'il nous a fourni sur commande, permettant de produire nos échantillons.

Je remercie Monsieur Idrissi et Monsieur Coulombier d'avoir accepté d'être lecteurs mon mémoire et de faire partie du jury lors de ma défense.

Merci à Mademoiselle Farzaneh Bahrami et Mademoiselle Sahar Jadi, pour avoir relu et corrigé mon mémoire. Leurs conseils de rédaction ont été très précieux.

Merci à mes parents, mes amis et mes chers colocataires, pour leur soutien constant et leurs encouragements.

List of acronyms

APS = ammonium persulfate CVD = Chemical Vapor Deposition
EBPVD = Electron Beam Physical Vapor Deposition
FIB = Focussed Ion Beam
HMDS = hexamethyldisilizane
MEMS = Microelectromechanical systems
LPCVD = Low Pressure Chemical Deposition
LOC = Lab On Chip
PMMA = Polymethyl methacrylate
PVD = Physical Vapor Deposition
RPM = Revolutions Per Minute
SEM = Scanning Electron Microscopy
TEM = Transmission Electron Microscope

Abstract

One way of producing graphene is by CVD growth on thin copper film, making it interesting to know the influence of graphene on the mechanical properties of copper. For this purpose, a process of a lab-on-chip uniaxial tensile test on copper/graphene with nickel actuators is determined. The results of this tensile test were compared with the results of lab-on-chip on copper and graphene separately. The interpretation of the results shows different things. 1. Nickel is not an ideal actuator, as it shows plasticity during actuation and relaxes over time. This makes the mismatch calculation with auto-actuated structures not accurate, the best solution is to measure the free beams. 2. Graphene has a real influence on the displacement measurements, its force contribution can not be considered as negligible. 3. The creep rate of copper/graphene seems to be higher than that of copper, due to poor adhesion between copper and graphene, a lack of measurements and a sample quality that needs to be improved. The average measured stress is lower for copper/graphene than for copper.

List of Figures

Contents

1 Motivation and context

Graphene is of great scientific interest, particularly in the field of renewable energy. Its properties never cease to amaze, leading to more and more ideas for concrete applications.

Its high electron mobility ($200,000\frac{cm^2}{Vs}$) and the high speed of electron movement within it ($1000\frac{km}{s}$) make it an ideal material for building ultra-fast transistors at the micron scale, which will heat up very little thanks to its immense thermal conductivity (up to $5300\frac{W}{mK}$).
Graphene is transparent, which makes it suitable for use in the manufacture of flexible displays and transparent electrodes.
By superimposing two layers of graphene in a suitable way (by adopting a relative angle of 1.1°), the material becomes superconducting.
Graphene could revolutionise batteries for energy storage. Indeed, its good conductivity, high mechanical strength and thinness of layer could increase tenfold the stored energy per unit weight on Lithium Ion batteries. Another possibility in energy storage is the use of graphene for the manufacture of super-capacitors with increased performance [17].

It is clear that graphene will be used extensively in the future, which justifies the study of its mechanical properties, both as an isolated material and in combination with other materials. This is with the aim of making it easier to manufacture, but also to make full use of its benefits in every application.

There are different ways of producing graphene films, and some of those involve the formation of graphene on copper thin films. It is thus of interest to characterize the way graphene influences the mechanical properties of copper. One should note that the mechanical properties of thin films are different from the properties of the bulk material. This is due to the effect of the grain sizes, morphology and orientation. Another factor is the small thickness that limits nucleation and motion of dislocations [18].

In this thesis, the feasibility of a mechanical test on a graphene/copper specimen is studied, with the aim of seeing how graphene affects the mechanical properties of copper. For this purpose, tensile tests are produced for graphene, copper and copper/graphene. In the first part of this work, the different ways of characterising the mechanical properties of thin films are presented. In the second part, the overall functioning of the tensile test that will be used in this work, the lab-on-chip, is explained. The process of lab-on-chip on graphene, copper and copper/graphene is detailed. In the third part, the data extraction method is explained. Results are extracted from the tests produced, those are compared with each other and conclusions are drawn.

2 State of the art on graphene mechanical testing

In this thesis, the influence of graphene on the mechanical properties of thin film copper is investigated. For this purpose, mechanical tests are performed on a film of graphene, copper and finally copper and graphene together.

This section includes:
1. The main processes for the production of graphene. The used process will have an influence on the quality of the graphene and on its mechanical response, therefore it is important to address this topic. The production process will also determine the macroscopic appearance of the graphene obtained (will it be deposited on a substrate, floating in a liquid under the form of small chips, with small or large crystals, etc). Knowledge of this is essential for the type of mechanical test to be used and the type of transfer to be performed.
2. The most common types of mechanical characterisation of thin films are described, in order to justify the one that will finally be used.

2.1 Graphene production

Graphene can be produced in many different ways. Each method has its advantages and disadvantages. The issues are the quantity of production, the size of the graphene crystals, the quality of the graphene and the cost of production. The most commonly used methods are exfoliation, epitaxy and chemical vapour deposition.

2.1.1 Exfoliation

Exfoliation is the mechanical peeling of graphene layers from a Highly Ordered Pyrolytic Graphite crystal (HOPG). It has been shown that this method can be used to produce graphene in a large scale and at low cost. To detach a graphene layer, different methods can be used to overcome the Van der Waals forces that bind the graphene layers together. These different methods have different effects on the structure and quality of the detached graphene. The graphite crystal can be solicited normally or laterally as shown on Figure 1.

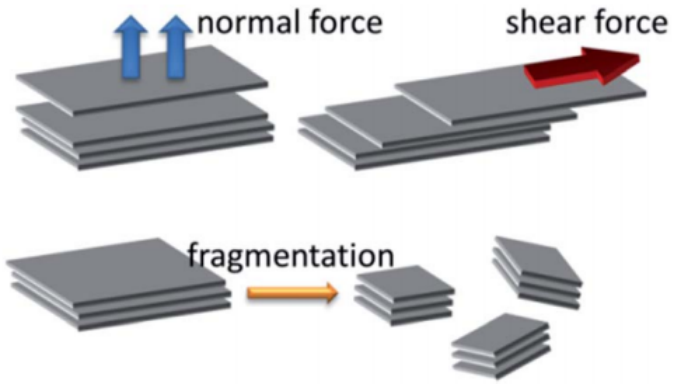

Figure 1: There are two kinds of exfoliation: normal force and shear force. Fragmentation should be avoided [1]

Yi & Shen [1] describe 4 methods of having exfoliation:

1. Micromechanical cleavage uses a Scotch-tape to detach the graphene layers from the graphite, with a normal force. This method is very time consuming and therefore doesn't look to be a candidate for industrial production.

2. The sonication method consists in the sonication and centrifugation of graphite powder in organic solvents. Sonification is at the origin of cavitation of the liquid around the graphite, which generates stress waves propagation into it, breaking it up into graphene layers. The centrifugation allows to increase the concentration of graphene left in the solvents. This is an easy way of performing exfoliation but so far, the graphene concentration in the mixture at the end of the exfoliation process is still very low (0.01mg/mL).

3. The ball milling method is focused on lateral forces to exfoliate graphite. While ball milling, two effects arise: the primary one is the shear effect, which has the tendency to detach large patches of graphene and that should be maximized. The secondary one is the fragmentation dominated effect, which breaks up the graphene patches into smaller fragments. This secondary effect should be minimized. Ball milling technique can thus be used for large-scale exfoliation of graphene, but the destructive secondary effect is unavoidable.

4. It is also possible to exfoliate graphene with fluid dynamics. The fluid (water or solvent) detaches layers of graphene by partial lifting and slippage. Vortex, pressure and speed variations of the fluid are parameters that could influence the quality of the graphene layer.

5. Two less investigated methods are:
   Detonation exfoliation where the shock-wave and the thermal energy cause violent exfoliation of the graphene.
   Super-critical fluid assisted exfoliation where a fluid penetrates the loopholes in the graphite, and is then suddenly expanded, leading to normal forces detaching graphene from the graphite crystal.

2.1.2 Epitaxy

The second method is epitaxy, where graphene is obtained by heating up a crystalline surface (for example silicon carbide) to 1300°C under vacuum. The silicon atoms on the edges of the wafer evaporate, leaving only carbon which reorganises into a graphene layer. This method has the advantage of not requiring a transfer, as the graphene is produced directly on the work surface. The result is a higher quality graphene, suited for electronic devices. But, large scale production is more difficult and is an expensive process [19].

2.1.3 Chemical vapor deposition

The third is the chemical vapor deposition (CVD) method, where carbonaceous gas is decomposed at high temperature on a metal catalyst substrate. The most commonly used catalyst substrates are copper and nickel. When growing on polycrystalline or monocrystalline nickel substrates, mono-layer

graphene is obtained up to 72.8% or 91.4%, respectively. The rest is multilayer graphene. This large difference is due to the grain boundaries of polycrystalline Ni. The use of copper as a substrate is more conclusive for the production of mono-layer graphene (up to 95%). This is due to the low solubility of carbon in copper, and to the fact that the deposition of graphene on copper is a surface reaction, preventing graphene from forming on top of a first graphene layer. The following considers the copper substrate as it offers better results for single layer graphene [20].

More technically, CVD can be performed at low pressure or at atmospheric pressure. For industrial production, low pressure production looks more difficult to perform as it involves multiple additional issues, such as unwanted evaporation of the metal substrate, a vacuum system that should be compatible with the flammable carbonaceous gasses. The CVD graphene manufacturing process at atmospheric pressures goes in four steps:

1. First, the copper substrate is placed at the midpoint of a horizontal glass tube about 1 meter long and 10 centimeter in diameter.
2. The second step is annealing and consists of gradually raising the temperature inside the tube from room temperature to 1050°C in 60 min and maintaining it for 4 min in an argon atmosphere. The aim is to reduce the residual fraction of carbon in the copper, which is not good for the quality of graphene.
3. The third step consists in removing the argon remaining from the annealing step by supplying a low H_2 concentration (<0.3%) in the tube for 20 min. It is important because the argon contains some oxygen, which would oxidize the copper. Directly introducing a high concentration of H_2 for the graphene growth without transitional step would lead to the reaction of H_2 with the copper oxide to form water vapour on the copper surface and cause its deterioration.
4. The fourth step is the growth of the graphene by introducing H_2 and CH_4 into the CVD furnace at a temperature of 1050°C and a pressure of 950 mBar.

Different parameters can be effective to increase the quality and size of the graphene domains. First, the way of placing the copper substrates in the furnace can be different. A common method is to put the wafers horizontally, but it takes up space, making it impossible to put a lot in at once. Then, it is possible to use a closely-packed vertically-standing wafers configuration inside the CVD furnace. The wafers are in the cross-sectional plane of the cylinder, which makes it possible to place wafers closer and in higher number. This way will make industrial graphene production easier [21; 22; 23]. A second parameter that can be effective is the carbonaceous gas flow and concentration inside the CVD furnace. As shown by B. Huet *et all*, reducing the gas flow is beneficial for the size of the graphene domains. They achieved domains of 2.6 mm. Figure 2 shows the effect of the concentration ratio between methane and hydrogen in the CVD furnace. From (a) to (h), the ratio H_2/CH_4 changes from 20 to 120 at constant methane flow.

As the thickness of graphene is around 0.335 nm thick and it is transparent, it is always handled in a stack with a supporting material. After graphene has been grown on a copper foil, it should be transferred on the wafer of interest with the method described in Section 3.2.2.

The CVD method has the advantage to produce good quality and large size of continuous graphene sheets, suited for electronic devices at low prices. Growth of graphene with CVD at atmospheric pressure is currently very promising for industrial production of graphene. Yet, the technology needs to evolve, in order to be able to control precisely various parameters such as the number of

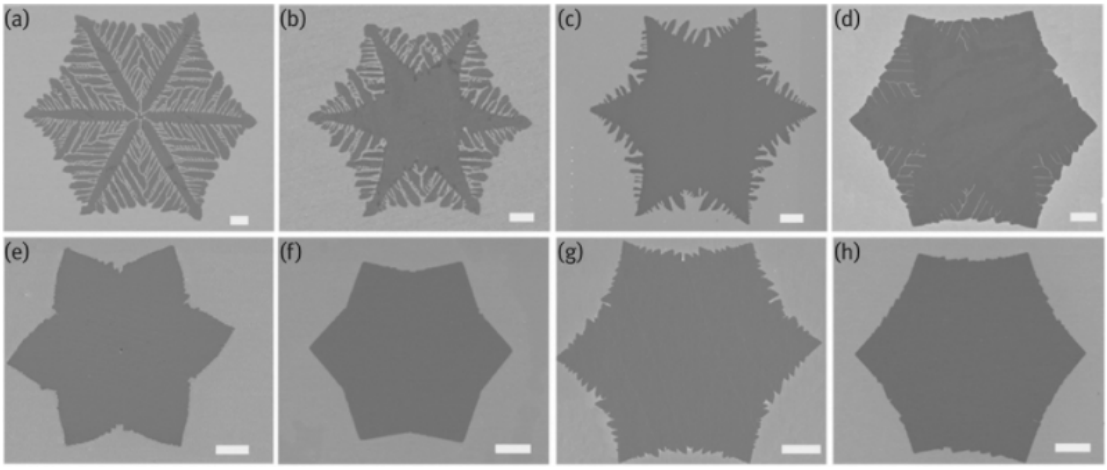

Figure 2: Different graphene domain shapes in function of ratio between H_2 and CH_4 in the furnace [2]

layers, the crystallinity, the deposition uniformity over large areas, the physical integrity and the surface planarity [23].

Of these three graphene production methods, epitaxy and CVD growth result in a graphene layer supported by a thin film. It will therefore be useful to be able to characterise the mechanical properties of a graphene layer and a thin film stacked on top of each other, as this is the configuration in which it is most handled and processed. In the following section, the different methods of mechanical testing of thin films are outlined.

2.2 On-substrate mechanical tests

In general, it is possible to test a thin film in two different ways: supported by a substrate, or freestanding in its environment. In this section, several on-substrate characterisation methods are described. Those methods usually can be performed with simpler procedures.

2.2.1 Nanoindentation

Nanoindentation is the most common method of mechanical characterisation. It is used to measure the hardness, young's modulus, creep and adhesion of a material. The principle of operation is to drive a tip into the analysed material until a maximum load (loading step), having a holding time at constant load (holding time) and when the displacement stops drive the tip out (unloading). During these three steps, the load is measured as a function of the penetration depth. The result is a curve shaped as Figure 3.

It is important to know the material and geometry of the tip, in order to take into account its deformations in the calculations. Usually, monocrystalline diamond is used as it is a very hard material that can not be deformed easily. The geometry of the tip depends on the application, but is most often a three-sided Berkovich type tip.

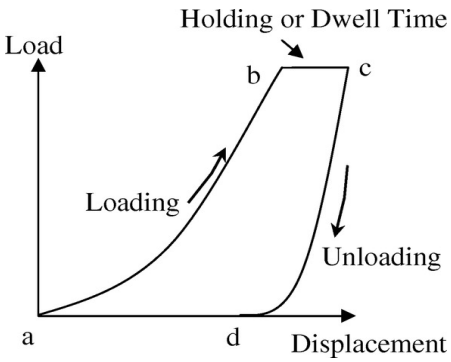

Figure 3: Load-Displacement curve of nanoindentation [3]

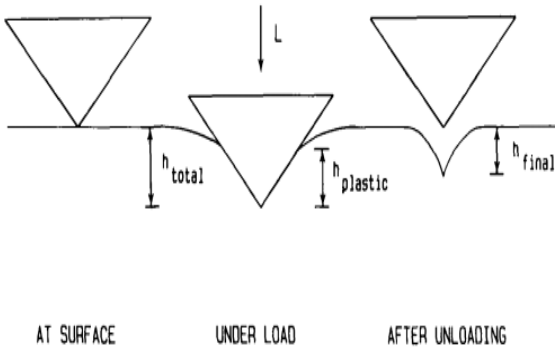

Figure 4: The three steps of nanoindentation [4]

The three indentation steps are shown on Figure 4. During the loading step, the material is both elastic and plastic deformed. During the unloading step, some sort of recovery is observed which is considered to be elastic recovery. The final depth remaining after the last step is due to the irreversibly of the plastic deformation. There is a difference between the total depth and the plastic depth. The total depth is measured from the initial surface level of the material, while the plastic depth is measured from surface in contact with the tip during indentation, which can be higher or lower than the initial surface level, depending on the material.

The hardness of the analysed material is defined as the load applied on the tip divided by the surface of contact of the tip with the material. The load P is known by measure, and the surface of contact can be computed knowing the shape of the tip and the plastic depth of penetration. Doerner and Nix [4] showed in 1986 that the plastic depth can be estimated from a line, tangent to the load displacement curve, through the highest load point. The intersection of this line with the x-axis is the plastic depth. This approach would be very accurate if the unloading occurred linearly, which is usually not the case. Olivier and Pharr [24] proposed in 1992 an improved technique to take into account the nonlinear behaviour of the unloading step. The contact area $A(h_{plastic})$ can be written in function of the plastic depth $h_{plastic}$ as:

$$A(h_{plastic}) = C_0 5 h_{plastic}^2 + C_1 h_{plastic}^1 + C_2 h_{plastic}^{\frac{1}{2}} + C_3 h^{\frac{1}{4}} + ... + C_8 h^{\frac{1}{128}} \quad (1)$$

For a perfect Berkovich indenter, $C_0 = 24.5$ and other coefficients are negligible. The hardness is defined as the ratio between the load and the contact area. The units are thus the units of pressure (Pa):

$$H = \frac{P}{A(h_{plastic})} \text{ [Pa]} \quad (2)$$

The Young modulus is extracted from the following relation between the known unloading stiffness $S = \frac{dP}{dh}$ and the known contact area $A(h_{plastic})$:

$$S = \beta \frac{2}{\sqrt{\pi}} E_r \sqrt{A(h_{plastic})} \quad (3)$$

β is a known dimensionless parameter, usually equal to 1. The reduced effective Young modulus E_r can thus be isolated. This reduced modulus is a function of both the modulus of the tip and of the analysed material, by a kind of average described in the following way:

$$\frac{1}{E_r} = \frac{1-\nu^2}{E} + \frac{1-\nu_0^2}{E_0} \tag{4}$$

The Young modulus E of the analysed material can finally be extracted, the other parameters being known (ν and ν_0 are the Poisson's ratio's of the material respectively the tip, and E_0 is the modulus of the tip).

Limitations of nanoindentation: thickness of the measured material should be high enough in order that the measurement is not perturbed by the substrate. The measurement depth should not exceed a certain percentage of the total material depth (usually between $\sim 1\%$ and $\sim 20\%$). The measurement depth should not be too small, because it would not give a realistic image of the material. This thus means that there is a minimal film thickness that can be characterized by nanoindentation, typically of about $100\mathrm{nm}$. Another limitation is the pile-up and sink-in effect, where the material, depending on if it is harder or softer than its substrate, starts to deform under the pressure of the indentor to form a bead or indentation, which changes the contact area and distorts the modulus calculations [25].

2.2.2 Wafer curvature thermal cycling

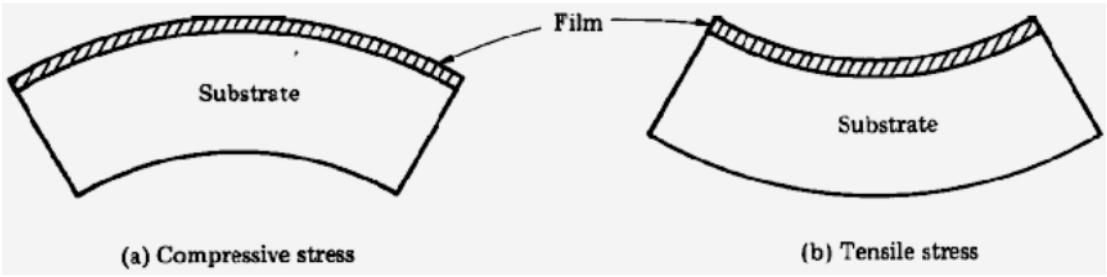

Figure 5: Curvature of thin film and substrate [5]

The study of thin films is usually done on a much thicker substrate as a working surface. This thin film is often deposited at a temperature above room temperature. As the materials often have different thermal expansion coefficients, the shrinking or expansion can occur in different ways while cooling. When handling this assembly at room temperature, the differences in stress/strain of both material will cause the assembly to bend. Depending on this difference, the analysed material will remain in compression or in traction (shown in Figure 5 (a) and (b), respectively)[26]. As the substrate is much thicker than the thin film, the thickness of the thin film can be neglected. In fact, to extract the stress in a thin film deposited on a substrate, there is no need to know any parameters of the thin film. One obtains the stress in the film σ by comparing the curvature radius of the wafer before and after the deposition of the film. This relation is described by the Stoney equation:

$$\sigma = \frac{1}{6}\frac{E_s}{1-\nu_s}\frac{t_s^2}{t_f}\left(\frac{1}{R_2} - \frac{1}{R_1}\right) \tag{5}$$

where E_s is the substrates Young modulus, ν_s the substrates Poisson's ratio, R_1 and R_2 are respectively the radius of curvature of the substrate before and after the deposition, and t_s and t_f the thicknesses of the substrate and of the thin film [27].

A limitation of the wafer curvature measurement for computing the internal stress is impracticability of measuring the stress locally. Stress gradient measurement is thus also not possible.

2.2.3 On-substrate uniaxial tensile test of films

Nanoindentation and wafer curvature characterise the thin films in three and two dimensions, respectively. This increases the complexity of the interpretation of the results, causing more inaccuracy. The simplest way to characterise a material mechanically is to have uniaxial tensile tests. Thin films are fragile, it is very complicated to manipulate them without substrate. Considering an on-substrate uniaxial mechanical test is a problem, because the substrate properties also influence the results. To have as accurate results as possible, soft substrates with known properties and low Young's modulus can be used. Chen, X. *et al.*[28] showed by determining the three dimensional elastic stress field in the substate that when the ratio of the moduli of both materials is less than 5, the error does not exceed 10%.

2.3 Freestanding thin films

When the thin film is freestanding, it is possible to study its properties more easily, as the result is not disturbed by any substrate. Freestanding thin film testing allows to go further in the plastic deformation regime, until the fracture. Different difficulties should be tackled: high precision on small forces, fabricating thin films in suspension, and making the connection between the actuator and the specimen. This section explores the main different freestanding thin films tensile tests.

2.3.1 Bending test

The bending test consists in bending a freestanding cantilever with a nanoindenter. This test allows to extract the mechanical properties out of a freestanding thin film. The ranges of the testing structures can be from a few microns till hundreds of microns length, and from nanometers to a few microns in thickness. The fabrication of the sample consists in deposition/transfer target film on a substrate coated with a sacrificial layer. It is then patterned in beams, and is followed by the sacrificial layer removal with a proper etchant. With a nanoindenter, a load is applied at the end of the beam, in order to bend it at a constant velocity (loading). At a certain point, the load is kept constant instead of the speed. The nanoindenter is removed (unloading) at the same speed as for the loading [29]. During that process (similar to the nanoidentation), the load applied and the deflection is recorded. The Young's modulus can then be obtained by reorganising the equation of the stiffness of a freestanding beam:

$$E = 4\frac{k(1-\nu^2)}{w}\left(\frac{l}{t}\right)^3 \tag{6}$$

where k is the stiffness of the beam, which can be obtained from the bending experiment as the slope of the load-displacement curve [25]. w is the width of the beam, t is its thickness, and l is its length computed from the very beginning of the freestanding part of the beam (the part that has been released) until the point of indentation. These measurements are complicated as it is not

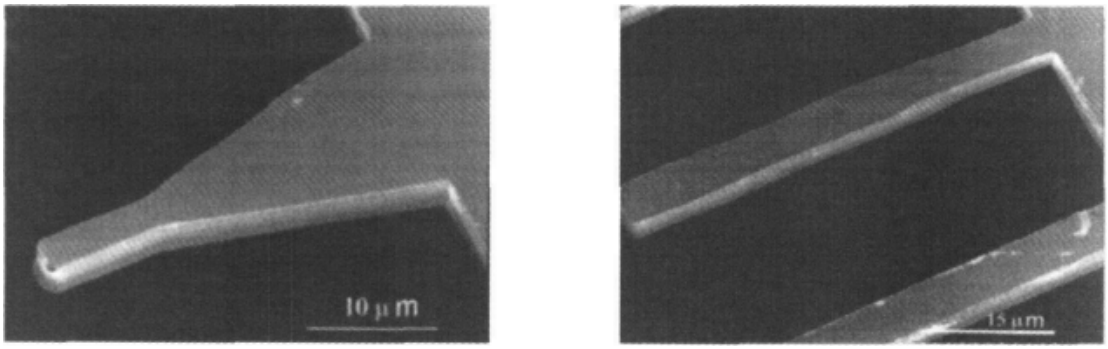

Figure 6: Triangular and rectangular beams [6]

always obvious until where the sacrificial layer has been etched under the beam. Yet, t and l should be accurate as they appear to the third power in the equation.

A weakness of this method for the first applied in 1988 is that the beam is not constrained uniformly. The bending is concentrated at the beginning of the beam when those are rectangular. To solve this issue, Florando F. *et al.*[6] proposed in 1999 to use triangular shaped beams. This method has the effect to distribute the state of strain uniformly over the length of the beam.

2.3.2 Bulge test

The bulge test aims at measuring the residual stress and the Young's modulus in an analysed thin film. As its name indicates, it consist in generating a bulge in the thin film using a pressurized fluid. Practically, the thin film is applied on top of an orifice and a uniform pressure is applied at the other side. The pressure differential over the thin film causes it to deflect, and this effect is measured in function of the pressure. A stress-strain curve can be plotted and the determination of the residual stress is possible. Vlassak & Nix *et al.*[30] applied this method for the first time in 1992. They used water as pressurizing fluid and pressures until 100kPa. The bulge deflection was measured with a He-Ne laser interferometer. Square thin films and rectangular thin films were used to measure different properties of the material.

- Square films were used to measure the elastic modulus. They obtained the results by applying number of loading cycles. The plastic deformation regime was not reached, so simply reconstructing the load-displacement curve suffices to compute the Young's modulus and residual stress. The latter is measured as the initial slope of the load-displacement curve.
- Rectangular films with low aspect ratio ($1 < \frac{length}{width} < 2$) validate the results of the square films. Rectangular films with high aspect ratio higher than two ($2 < \frac{length}{width}$) give accurate results for the Poisson's ratio of the thin film. This property describes in what extend the material expands or shrinks in the perpendicular direction of loading.

Jay S. Mitchell *et al.*[31] validates the previous study by comparing it with others studies (Pan *et al.*(1990)[32] and Maier-Schneider *et al.*(1995) [33]).

The linear elastic analysis of the sample is not valid anymore once the plastic deformation regime is attained. If the film subjected to a uniform pressure is an infinitely long rectangle (high aspect ratio), it will look like a cylinder (see Figure 7) and it will be possible to model it as such. If the deflections remains small ($h << a$), the stress and strain in the thin film can be written as [7]:

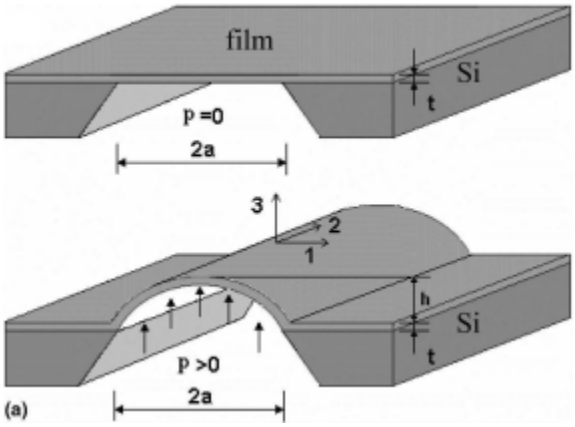

Figure 7: Plane strain bulge test on a long rectangular membrane Xiang, Chen and Vlassak (2005) [7]

$$\sigma = \frac{pa^2}{2ht} \qquad (7) \qquad\qquad \epsilon = \epsilon_0 + \frac{h^2}{3a^2} \qquad (8)$$

where *a* is the half of the width of the cavity, *h* is the deflection distance, *t* is the thickness of the film, and *p* is the applied pressure. ϵ_0 is the residual stress in the film.

Limitation of this method is that the results are very sensitive to the dimensions of the thin film on top of the cavity. The accuracy of the test sample preparation is thus very important. Jay S. Mitchell *et al.*underlined the importance of having a very accurate process and precise measurements of thickness and width of the samples. They concluded that uncertainties of 6.5% and 8.5% for the residual stress of mono and polycrystalline SiC. 7% and 9% uncertainty was found for the Young's moduli.

2.3.3 Uniaxial tensile test

Obtaining the mechanical properties of a thin film is not an easy task. The methods mentioned in the previous sections provide a means of calculating the properties of the analysed material in two axes, but the subsequent data processing is more complicated and less accurate. The most direct method of calculating material parameters is uniaxial stress testing.

These tests are not easy to perform due to the fragile nature of thin films, that have thicknesses of the order of a few microns to far below. The testing methods must combine micrometric motor displacement while keeping force measurement precise. Here is a non-exhaustive list of the latest studies that have been carried out on the subject.

In 1997, Sharpe *et al.*[8] developed a method to measure the Young's modulus in a direct way, consistent to its definition. They made a proof of concept by analysing phosphorus-doped poly-silicon, deposited by low pressure chemical vapor deposition (LPCVD) on a silicon substrate. Beams of $4\ \mathrm{mm}$ long and $6\ \mathrm{mm}$ wide are patterned using standard fabrication methods (lithography, etc) in the $3.5\ \mu\mathrm{m}$ thick poly-silicon layer. Two gold strips are deposited in the middle of the length

of the specimen, in order to be able to measure the displacement accurately with a laser beam. Two gold strips can also be deposited in the width, in order to measure the changes in width when the sample is loaded. This measurement allows to compute the Poisson's ratio. Then, a cavity is etched under the specimen to release it from the substrate. The sample is then clamped between two grips, one is fixed, the other is actuated by piezoelectric motors. The sample is glued in the clampers to keep it in place. Finally, the two support strips are cut away to have only the sample between both clampers. Figure 8 represents a SEM image of the released beam, from a certain angle.

Figure 8: SEM image of the released specimen (Sharpe *et al.*[8])

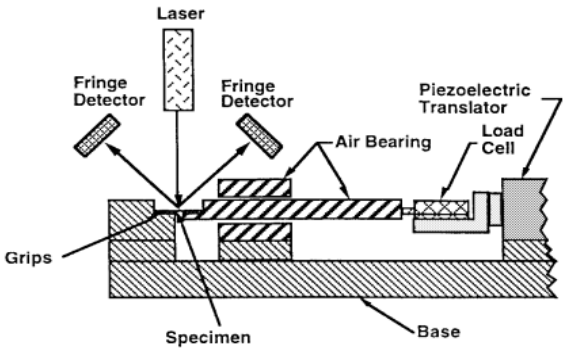

Figure 9: Setup of the measurement bank (Sharpe *et al.*[8])

Figure 9 shows the setup of the experiment. The laser and the fringe detectors measure the displacement, from which the strain can be computed, while the load cell measures the load applied by the motor on the sample. From those measurements, the load-strain curve can be plotted. The air bearing is there to eliminate friction forces.

It is to note that fatigue test can also be done on the sample. The laser uses two fringe detectors to provide accurate resolution of 5 microstrains. The Young's modulus can be measured with an accuracy of 3.9% while the fracture strength with 13%.

Adhesive gripping systems are not ideal because the sample is difficult to remove after the test and mechanical grip is difficult to use for thin films because they are so fragile. In 1997, Tsuchiya *et al.*[9] proposed a new tensile tester to tackle that issue. The new tester is using an electrostatic-force grip.

The electrostatic gripping system works by charging the probe at certain moments. The probe is made of a conductor material, coated with an insulating film on the surface that comes in contact with the substrate. First, the probe is placed on top of the specimen. Then, a voltage is applied between the probe and the specimen. This creates an electrostatic force between them, normal to the direction of the load. Thanks to static friction force, a load can be applied on the probe to pull on the sample. Once the sample is broken, an inverse voltage is applied between the probe and the substrate. This causes the broken piece of the specimen to be attracted by the substrate and fall down from the probe. Thanks to this method, it is possible to repeat the tensile test on different specimens without having to stop to clean the gripping system from its glue.

The tensile tester was built in the chamber of a SEM, allowing in situ observation of the sample. It is actuated by both a stepper motor and a piezoelectric motor for the fine adjustments. The proof

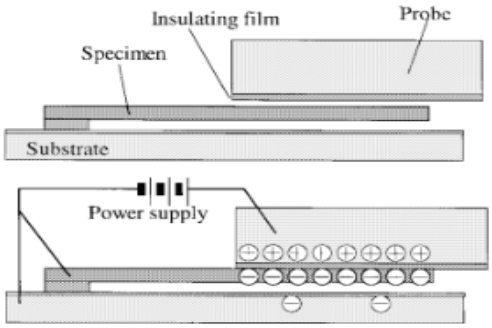

Figure 10: Electrostatic force gripping system, step 1 and 2 (Tsuchiya *et al.*[9])

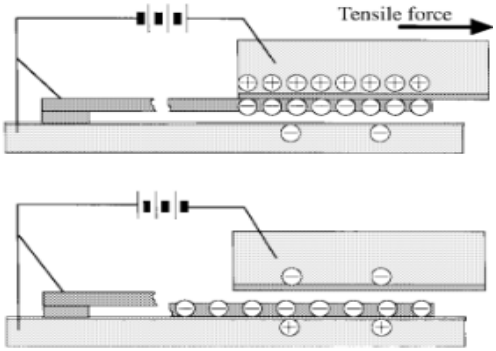

Figure 11: Electrostatic force gripping system, step 3 and 4 (Tsuchiya *et al.*[9])

of concept was done for a thin polycrystalline silicon film with dimensions of 30, 100 or $300\mu m$ length, 2 or $5\mu m$ wide and $2\mu m$ thickness. One drawback of this method is that is it limited to conducting materials.

In 2001, Read *et al.*[10; 34] presented a new uniaxial tensile test for thin films. They showed the validity of the new method by applying it on aluminium thin films. Aluminium was evaporated with electron beam and deposited on a silicon wafer. It was then patterned in beams of 180 μm long by 10 μm wide with standard fabrication techniques. One side of the beam remains attached to the substrate, the other side is shaped in a tab, with a hole in the center. The tab is connected to the substrate by tethers to keep it in place (see Figure 12). Then the beam, the tethers and the tab are released from the substrate by dry etching (with XeF_2) until a depth of 50 μm.

The actuation occurs with a hook mounted on a three directional piezoelectric stepper motor micro-manipulator. The latter allows to displace the hook at the speed of 0.3 μm. A force sensor with a calibrated force range of 20 mN is mounted on the hook. Before actuating the sample, it is needed to break the tethers with the hook. It can then be inserted in the hole in the tab in order to load the sample.

Haque *et al.*showed a new uniaxial tensile test involving Microelectromechanical systems (MEMS) force sensors in 2002 [11]. The new method has some advantages in comparison to others. As it is all on chip, there is no need for complex gripping machines to load the sample. The small setup size of the test allows freestanding film's mechanical properties to be measured in situ in Scanning Electron Microscopy (SEM) and Transmission Electron Microscopy (TEM). It also makes possible to measure the pre-stress in the specimen. The load and the specimen are aligned with good precision thanks to the lithography. Lastly, it is possible to measure the creep strain in the material. The method was validated by characterizing aluminium freestanding beams of 275 μm long, 8.8 μm wide and 100 nm thickness.

Figure 13 shows the test chip. The left part is fixed, the right part is glued on a piezoelectric motor that acts as actuator. One observes that the pulling end is connected to the fixed end by 'U' shaped connectors for structural integrity of the total. The 8 supporting beams are there to make sure the load is applied in the same direction as the specimen. Cursor B is used to measure the displacement of the loaded specimen. Cursor A gives an indication on the displacement of the force

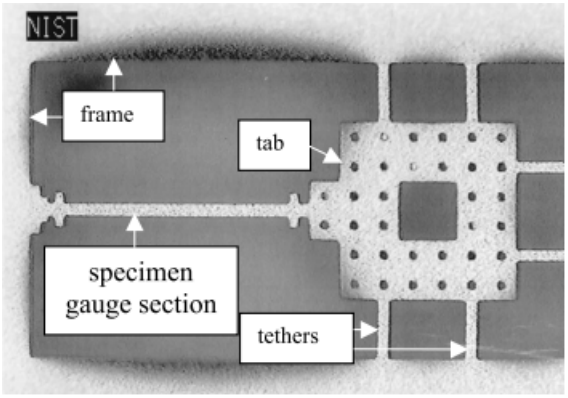

Figure 12: SEM image of hook actuated uniaxial tensile test (Read *et al.*[10])

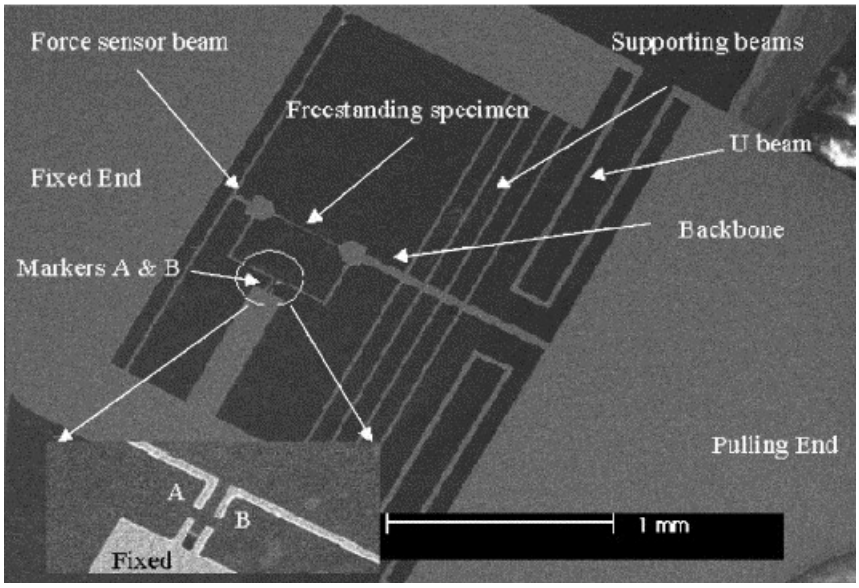

Figure 13: Uniaxial tensile test integrated MEMS force sensors developped by Haque *et al.*[11]

sensor beam. This force sensor beam is a silicon beam with a known spring constant (determined from its geometry, here 27.9 N/m). If the displacement is measured, the force can be computed. Measuring the displacement before loading the specimen allows to compute the tensile pre-stress in the specimen.

Espinosa *et al.*(2003) [12] showed an interesting new way of measuring the mechanical characteristics of thin films. It consists in loading a horizontal suspended thin film by applying a vertical force in the middle of the specimen with a nanoindenter. The specimen is fixed at both ends and has an enlargement in the center in order to be stronger at this place and to not deform there. The tip of the nanoindenter is line shaped in order not to break the sample. The displacement is measured

with a Mirau microscope interferometer, which is placed under the sample.

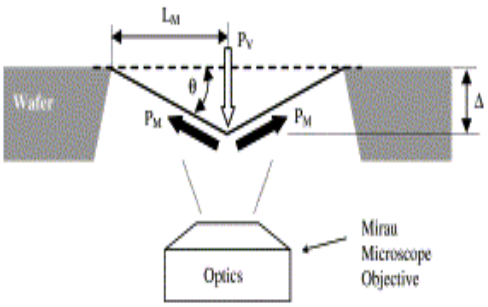

Figure 14: Setup tensile test (Spinosa *et al.*[12])

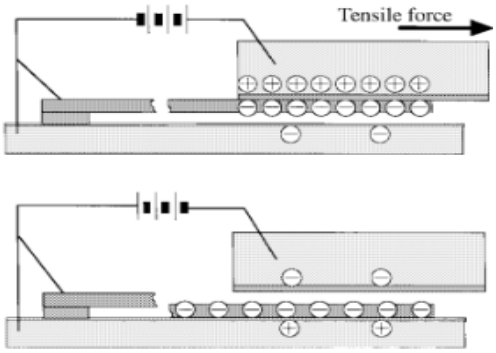

Figure 15: Dog bone shaped gold specimens (Spinosa *et al.*[12])

For the fabrication, a silicon wafer with Si_3N_4 deposited at both sides is used as substrate. The gold specimens are deposited in liftoff mode after the deposition of a very small Ti layer to improve the adhesion. The specimens are designed in a double dog bone shape, attached at both sides to the substrate. The dogbone shape in the center of the specimen is designed to receive the nanoindenter in order to reduce the stress concentration at the point of contact. At the attachment with the substrate, the specimen is also wider, in order to minimize the stresses at the point of folding. In this way, the narrow part of the specimen (the one that should be extended) is only constrained by direct tension. After deposition of the specimen, a window is back etched in the silicon wafer, with some techniques to prevent the etchant to reach the gold specimen.

The advantage of this method is its simplicity, and the fact that the measure of the stress and strain are independent (the first one is done thanks to the nanoindentor force sensor, the second one via the interference microscope). Different materials can easily be tested with the same technique.

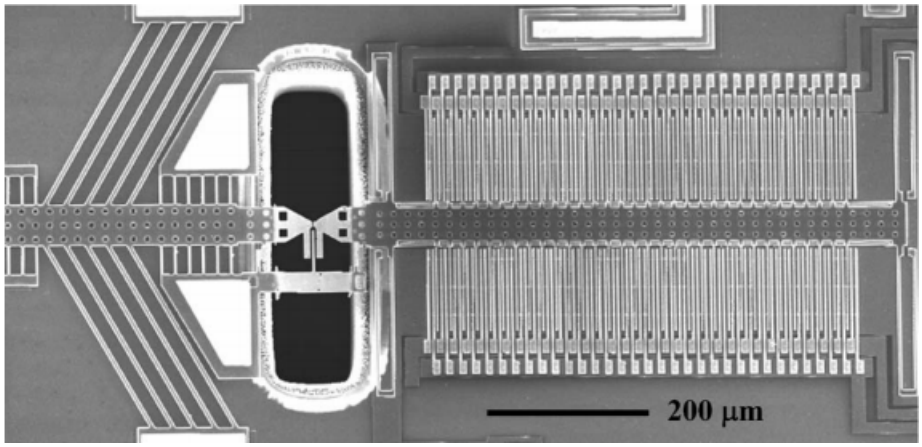

Figure 16: Electrothermal actuated tensile test (Espinosa *et al.*[13])

In 2007, Espinosa *et al.*[13] showed a new way of testing thin films. The design includes an actuator and a load sensor. The in-plane thermal actuator enables to control the displacement. It consists of the 'V' shaped beams on the left of the device (see Figure 16). A voltage is applied across them, causing a current to heat them up via Joules effect. This causes the 'V' shaped beams to expand, pushing the left actuator to the left. The load sensor is based on differential capacitive sensing of displacement. The sensor is made of a set of mobile fingers, and a double set of fixed fingers. When the sample is loaded, the mobile fingers displace, changing the capacitance between movable and fixed fingers. If the device is calibrated carefully, it is possible to extract the displacement from the measured variations in the capacitance.

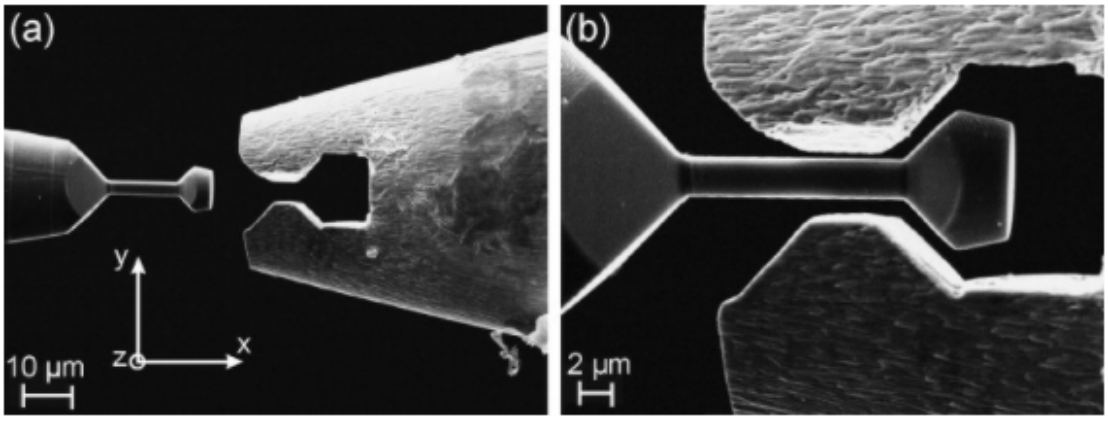

Figure 17: Tensile test shaped with FIB by Kiener *et al.*[14]

Kiener *et al.*[14] proposed in 2008 a new method for in situ testing of thin films. It consists in shaping the sample and the gripper to complementary forms, so they can be attached and actuated.

More specifically, to construct the copper sample, they started from rods with dimensions of 20 mm by 0.5 mm by 0.5 mm, cut with a diamond wire saw. It is then shaped into a tip with electrolyte and lastly cut with Focussed Ion Beam (FIB) in the shape shown in Figure 17. The tensile test was performed directly after the milling, in a SEM and actuated with a tungsten gripper that fits on the sample shape (see Figure 17), actuated by a micro-manipulator. During the actuation, load and displacement are measured and SEM images were taken.

Different sample shapes were tested. The aspect ratio was varied between 1:1 and 13.5:1. The experiments demonstrated that high aspect ratios show single slip deformation, negligible hardening and a moderate dependence of the flow stress on the sample size [14].

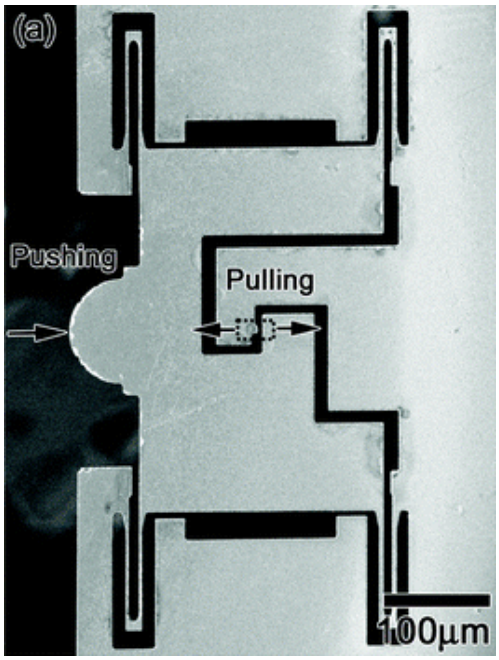

Figure 18: Push to pull tensile device for testing VO_2 nanowires (Guo, Chen *et al.*[15])

It is worth noting the push-to-pull method, which was used in many recent studies on tensile properties of thin films such as VO_2 nanowires, Mo alloy nanofibers, helium and Sulfur Ion-Irradiated BCC iron and polymer films, respectively analysed by Guo and Chen *et al.*(2011), Chisholm *et al.*(2012), Kundu *et al.*(2020) and Velez *et al.*(2021) [15; 35; 36; 37]. The main advantage of this tensile device is the visibility from of the specimen from both sides of the sample. This enables the use of transmission electron microscope to study the changes in the material structure, such as dislocations.
Beside of that, the push to pull testing method is a way of avoiding the difficulties associated with the gripping of the thin film. Instead of gripping the film with a gripper or by gluing it to an actuator, the thin film is transferred with a micro-manipulator on a push-to-pull device as shown on Figure 18. To increase the adherence of the thin film on the device, it is common to weld it with platinium. The push-to-pull device is made of silicon. The 4 'U' shaped beams are present for avoiding any lateral displacement of the mobile part of the device. For the actuation of the thin film, the push to pull device should be pushed with a pico-indentor on its left side, leading to a tensile load in the thin film. The pico-indentor has an integrated force/displacement sensor [38].

3 Lab-on-chip uniaxial tensile test

The techniques exposed in the state of the art are varied and each requires its own degree of expertise. However, they all have in common that they depend on an external input to function, it can be a current, a pressure, a nanoindenter or a micromanipulator. Often they are also only applicable on a small scale and are expensive in terms of set-up time. In this section a new mechanical characterisation technique developed in 2009 at UCLouvain by Gravier, Coulombier *et al.*[39] is presented. The first subsection (3.1) describes the global working of the lab-on-chip (LOC). The second subsection 3.2 treats the general fabrication steps that are used to manufacture LOC. In the third and fourth subsection (3.3 and 3.4), the process that was developed to manufacture LOC on graphene and on graphene/copper is detailed. Finally, Section 3.6 explains the process problems encountered to manufacture LOC for different specimen and how they were resolved.

3.1 Working of a lab-on-chip

The lab-on-chip is an all integrated, on chip uniaxial tensile device for freestanding thin films. The principle of actuation is to use the internal stresses present in one material to actuate the second. To achieve this, three layers of material are needed on a thick substrate as working area. In conventional LOC, the first layer is the sacrificial layer, deposited on the whole substrate and without any patterning. The second layer is the analysed material, called the specimen. It is deposited on the whole wafer and patterned in specimen beams of 1-8 microns wide on 20-800 microns length. The last layer is the actuator layer, which presents high internal stresses. It is deposited over the whole wafer and patterned in actuator beams of 11 microns wide on 50-1500 microns length. The actuator beams and the specimen beams have an overlap. One specimen beam and one actuator beam together forms one tensile test structure. On a single wafer, thousands of test structures can be processed at once. It should be noted that the actuator can also be deposited first, depending on the properties of the materials used. The dimensions can also vary.

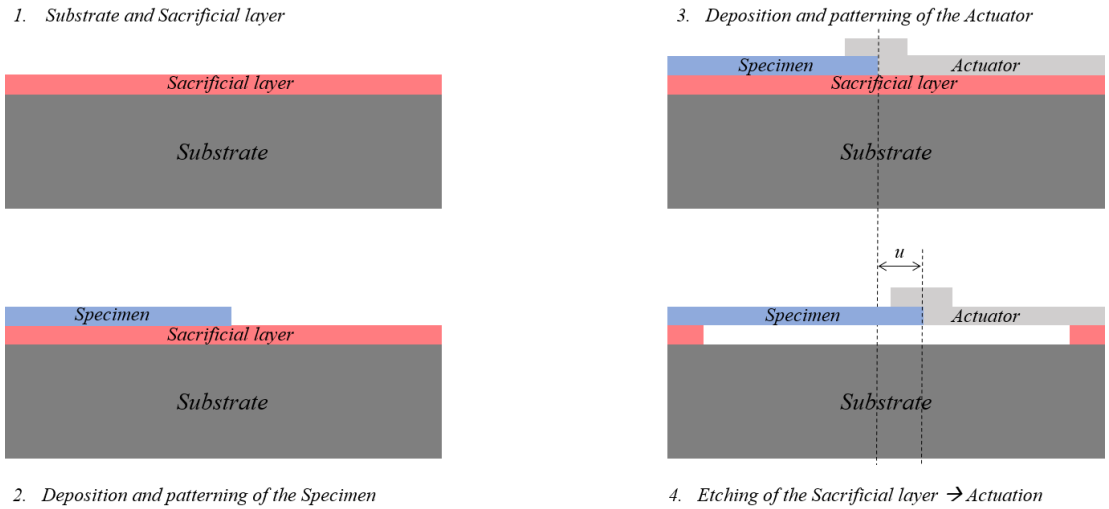

Figure 19: Operating principle of the lab-on-chip

In order to extract data from the test structures, those are released by etching away the sacrificial layer with an etchant solution. Once released, both the specimen beam and the actuator beam are freestanding. The actuator beam is delivered from its internal stresses and pulls on the specimen beam. Finally, the displacement u in the test structure can be measured under the SEM microscopy.

3.2 General process steps

In this thesis, LOC on three different materials which act as specimen beams have been investigated: Graphene, Copper and Graphene/Copper. The type of material chosen as specimen can effect the process, but some steps stay the same. This subsection describes the general steps that are the same regardless of the type of specimen. The temperatures, timings, rotation speeds that vary in function of the case are specified in Appendix A and B for graphene and copper/graphene specimen respectively.

3.2.1 Standard cleaning

All the processes begin with the standard cleaning, which aims at cleaning the silicon wafers and guaranteeing the absence of any contamination or oxidation on the wafer that can influence the process. It consists in plunging the wafer in baths of Piranha, which is a mixture of sulfuric acid (H_2SO_4) and hydrogen peroxide (H_2O_2). As a strong oxidizing agent, Piranha is able to dissolve most organic matter. After having rinsed it with water, the wafer is put for 15 seconds in a 2% hydrofluoric acid (HF) solution in order to remove the oxide layer on the silicon (SiO_2) and is again rinsed in different baths of water. Finally, the wafer is dried in a centrifugal spin dryer. The wafer needs to be completely dry for next steps.

3.2.2 Graphene Transfer

Graphene transfer is a critical step in the sample preparation process. Its fragility requires the utmost care in its transfer. The transfer of graphene is detailed in Figure 20 in five steps.

Figure 20: Graphene Transfer steps

1. The first step is the growth of high quality graphene sheet by CVD on copper substrate, as explained in Section 2.1.3. Graphene sheets have dimensions of around 3 cm by 3 cm. This

step is performed in the clean room of UCLouvain.

2. Step two is the coating of a protective layer of Polymethyl methacrylate (PMMA) of around 500 nm on top of the graphene.

3. In a third step, the sheet is placed on the surface of a $FeCl_3$ solution to dissolve the copper foil. 10 minutes is enough to remove the copper, then the $FeCl_3$ solution is gradually replaced by water. The graphene and PMMA stack is left floating on regularly replaced water for 5 hours to be sure no $FeCl_3$ is left on the graphene.

4. The actual transferring step of the graphene+PMMA stack, floating on the surface of the rinsing water, requires precision. Two methods were used, the first one consists in 'fishing' the floating graphene and PMMA stack with the wafer of interest. When transferring graphene on cavities or thin film copper, this method cannot be used as water can be trapped between cavities and graphene. The water trapped could vaporize while drying and cause the rupture of the graphene sheet. The water could also cause the oxidation of the copper surface. The second approach of transferring is the paper transfer, which is preferred when the substrate is coated with copper film or contains cavities. It consists in placing a paper sheet on the floating graphene and PMMA stack, which will stick to the paper. The stack of paper/PMMA/graphene is then kept for a while at room temperature to vaporize the water from the graphene surface, and then it can be placed on the target substrate. The graphene and PMMA stack then separates from the paper and sticks to the substrate. Figure 21 shows copper that has been oxidized because of water trapped between itself and the transferred graphene. The black dots in Figure 22 are due to contamination by $FeCl_3$.

Figure 21: Oxidation of copper because of the presence of water between substrate and graphene

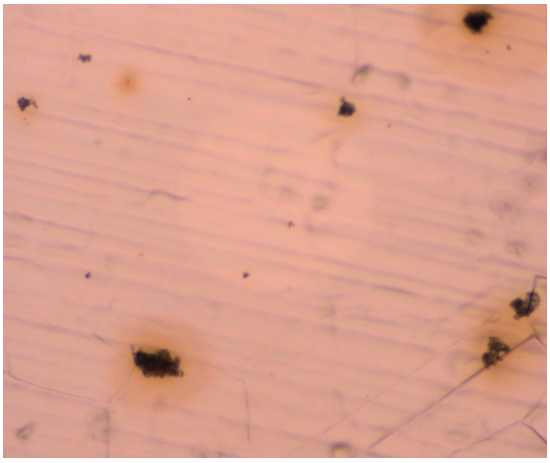

Figure 22: Contamination of the copper thin film by $FeCl_3$ residues on the graphene

5. The fifth step consists in removing with acetone the supporting layer of PMMA. To facilitate this step, a fresh layer of PMMA can be coated on the old layer. Then the stack is placed in acetone at 60°C to remove both PMMA layers.

3.2.3 Positive lithography

The positive lithography aims at patterning the specimen part of the structure on the wafer. The principle is to protect with resist the part of the specimen to be kept, and etching away the non-protected parts with a gas, a fluid or an ion beam. This process goes in four steps enumerated below and shown in Figure 23.

1. The first step consists in spincoating the positive resist on the wafer with the deposited copper film. This is done by first putting the sample in the LPIII oven for 30 minutes to improve the adhesion on the surface of the wafer at a temperature of 120°C in an hexamethyldisilizane (HMDS) environment. This helps to have a good adhesion between the resist and the substrate. Then, the wafer is spincoated with positive resist with a thickness depending linearly on the rotation speed of the coating. Lastly, the resist is baked in the oven to harden it.

2. The second step consist in pattering the photoresist by exposing it to light. At first, in order to have the desired pattern, a lithography mask is put on top of the wafer. This mask is transparent where the light is desired to destroy the photoresist, and opaque where the resist should stay. If the patterning is the first one and that the specimen does not risk to stick to the mask, vacuum contact can be used to improve the resolution. The wafer is exposed through the mask. The intensity of exposition varies with the thickness of resist and plays an important role in the resolution of the patterning. Once the resist has been exposed, the wafer is post baked and then developed, to remove the soft, exposed resist.

3. The third step is the removal of the non protected thin film. For graphene, an O_2 plasma is used. To remove copper, ammonium persulfate (APS) is be used.

4. The last step is the dissolution of the photoresist remaining on the wafer. This is done with acetone at 60°C.

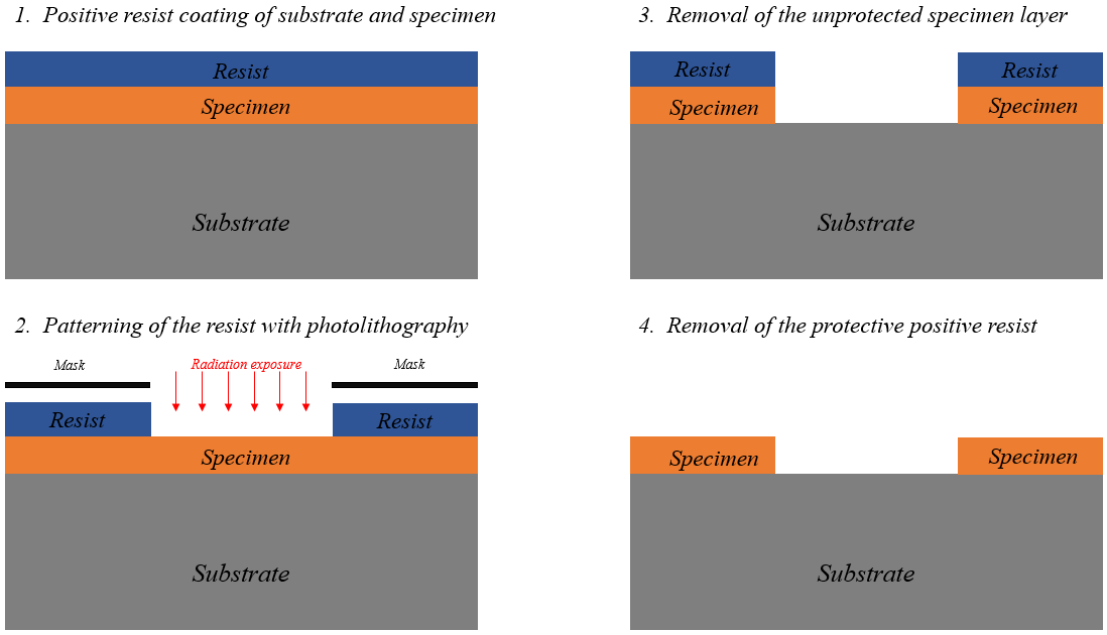

Figure 23: Positive lithography

3.2.4 Negative lithography

The negative lithography is used to pattern the actuator part of the test structure on the substrate. The principle is to pattern the lift-off resist on the wafer where no actuator is supposed to exist. In this case, the actuator is of nickel. After patterning the coated resist, nickel is then deposited everywhere, and lastly the underlaying resist is removed, taking with it the non-desired layer of nickel. The method is very similar to the positive lithography and also goes in four steps, enumerated below and shown in Figure 24.

1. The first step consists in spincoating negative resist on the wafer. It is done in exactly the same way as for positive lithography, except the rotation speed, time and temperatures that vary slightly. Those parameters are given in the next subsections (3.3 and 3.4), according to the case.

2. The second step consists in patterning the photoresist by exposing it to light. A mask is also used but for negative resist, it goes inversely: The parts that are lighted become stronger and are not removed by the developer. The wafer is exposed through the mask. The intensity of exposition varies with the thickness of resist and plays an important role in the resolution of the patterning. Once the resist has been exposed, the wafer is post baked and then developed, to remove the soft, non-exposed resist.

3. The third step is the deposition of the nickel thin film everywhere on the wafer. This should imperatively be done in lift off mode, as explained in 3.2.5

4. The last step is the lift off. It consists in dissolving the resist under the nickel to remove it. This is done with acetone at 60°C.

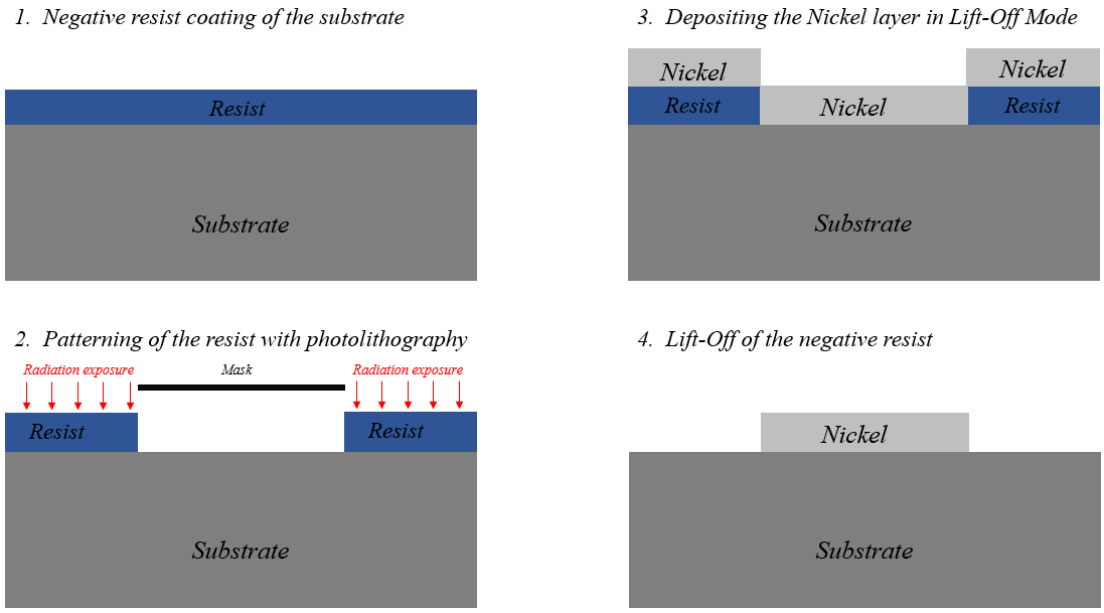

Figure 24: Negative lithography

3.2.5 Physical vapor deposition

Physical vapour deposition (PVD) describes a wide range of vacuum deposition methods that enable the growth of thin films on a substrate, atom by atom. It is characterized by vacuum deposition methods in which a material starts from its condensed phase, is vaporized in the vacuum environment and then re-condensed on the substrate, forming a thin film [40]. Among the different PVD methods, one of the most used is the electron beam evaporation PVD, used for producing pure metal thin films such as copper and nickel. In this purely physical process, the metal is evaporated from the crucible (the source) by heating it at high vapour pressure with an electron beam under vacuum ($10^{-2}\ Pa$). The high kinetic energy electron beam is generated by a hot tungsten filament and deviated by an electromagnetic field on the crucible. Atoms evaporated from the source deposit on the substrate, forming a thin film.

The wafers are placed perpendicular to the flow of evaporated atoms, which reach them in the normal way, somewhat like snow falling vertically on a ledge (Figure 25, a). This is called the Lift-Off mode. To make the deposited layer more homogeneous, it is possible to rotate the wafers relative to the direction of flow during deposition. The atoms then arrive on the surface from all directions (Figure 25, b). This is called rotate mode. In the case of cavities in the wafer, it can be seen that in the latter case the atoms are deposited on the bottom of the cavities as well as on the vertical walls [41]. When depositing for negative lithography, the liftoff mode must be used, otherwise the film deposited on the walls prevents the acetone from detaching the resist and the unwanted layer. When using rotate mode in the presence of cavities in the wafer, it can be seen that the atoms are deposited on the bottom of the cavities as well as on the vertical walls.

In the case of lab-on-chip, knowledge of the internal stresses within a film is crucial to be able to derive information from a sample. This is why an extra wafer is always used for PVD, inorder to

calculate internal stresses, by curvature measurement before and after deposition using profilometry.

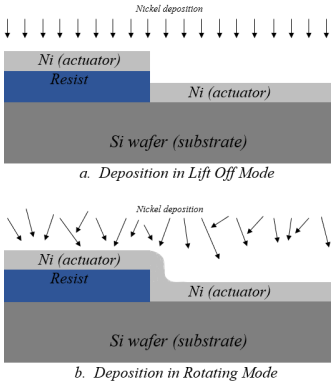

Figure 25: (a) Lift-Off mode and (b) rotating mode

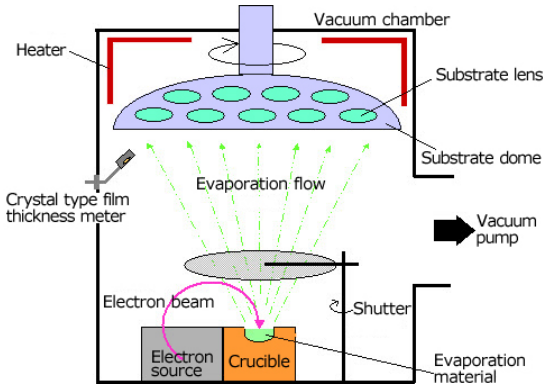

Figure 26: Scheme of the electron beam evaporation [16]

3.2.6 XeF_2 dry etching

The last step of the process is the release, where the sacrificial layer of silicon is removed from under the test structures. The method used is dry etching, where Xenon difluoride gas (XeF_2) is used. This isotropic process allows the etching of silicon with almost infinite selectivity from silicon to photo resist, silicon oxide, silicon nitride and aluminium. XeF_2 has a vapour pressure of 4 Torr (533Pa). The reaction that takes place is as follows:

$$2XeF_2(g) + Si(s) \rightarrow SiF_4(g) + 2Xe(g) \tag{9}$$

The etching rate of the monocrystalline silicon used as a sacrificial layer by XeF2 is 460-700 nm/min. The apparatus used for etching has three chambers: The first contains XeF_2 crystals at atmospheric pressure. The second is the expansion chamber. The third is the etching chamber [42]. The sample is placed in the etching chamber, which is evacuated ($P =\sim 10$ Pa). To deliver a pulse of gas to the sample, the expansion chamber is evacuated and brought into contact with the chamber containing the XeF_2 crystals, at atmospheric pressure. The pressure in both chambers drops below the vapour pressure of the XeF_2, allowing some of the crystals to sublimate. The gaseous XeF_2 disperses into the expansion chamber. By controlling the contact time of the two chambers, the amount of gas in the expansion chamber is controlled. All valves are closed, and the expansion and etching chambers are then brought into communication with each other. The XeF_2 pulse acts for a few seconds and then the whole system is evacuated with an abundance of nitrogen [43; 44]. As the etching power of XeF_2 is high, the use of several small pulses of XeF_2 (300-400 Pa) briefly (10 s) submitted to the etching chamber is recommended.

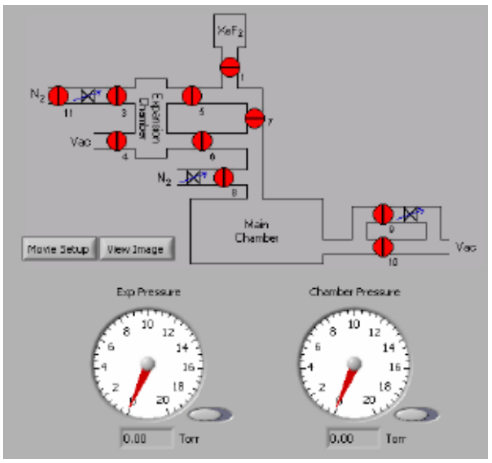

Figure 27: XeF_2 apparatus scheme

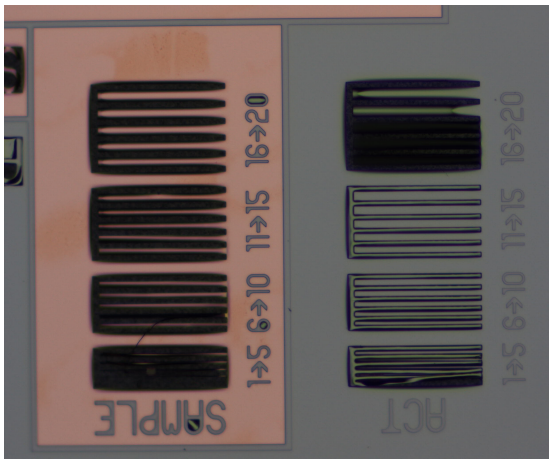

Figure 28: Release structures

In the case of the lab-on-chip, the distance to be underetched is that of a half-actuator as the etchant comes from both sides of the actuator, which are until $15\ \mu m$ wide at their widest places. As the etching is sometimes not homogeneous, more than the half-actuator is etched to be sure all structures are well released. One usually chooses to release until $14\ \mu m$. To estimate the underetch distance of the silicon under the nickel which is opaque, dedicated structures are observed between each pulse. These structures have increasing widths and go out of plane or deform when released. An example of these release structures is shown in Figure 28, where the structures have been released until structures wide of $18\ \mu m$. Silicon that has been in contact with XeF_2 turns black because its surface becomes porous and rough and reflects light in all directions. One notices that the lift-off was not perfect and that the 10 first actuator structures are still under nickel.

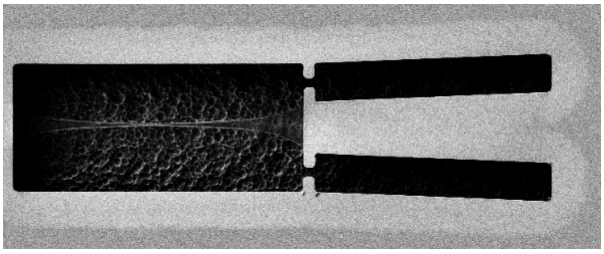

Figure 29: Graphene actuated by nickel LOC with visible underetch

It is important to wait for the vacuum at the beginning of the process, to be sure that the water has been completely evaporated.If any water remains the following reaction takes place, leading to the production of HF, the same acid as for standard cleaning.

$$2H_2O + 2XeF_2 \rightarrow 0_2 + 2Xe + 4HF \tag{10}$$

Finally, it should be noted that the resulting wafer, three inches in diameter, is too large to be released in one go. The small amounts of XeF_2 contained in each pulse would be outnumbered by

the amount of Si present in the chamber, leading to non-uniform etching.Releasing a whole wafer at once would not make much sense, as it is preferable to measure the structures directly after release. Since a single wafer contains thousands of structures, it would be impossible to measure them all in the hours following release.

3.3 Process LOC Graphene

In this subsection the process used for lab-on-chip on graphene is detailed. The six main steps are shown in Figure 30. The various parameters of each step are summarized in a table in Appendix A.

- Step a) is the standard cleaning of the wafer, as explained in Section 3.2.1. The monocrystaline wafer used has a diameter of 3 inches and a thickness of 380 μm. The upper surface is polished. A wafer with a monotonic profile is preferred since a curvature measurement by profilometry is used to calculate the internal stress in the deposited films.

- One of the difficulties in studying graphene is its transparancy, which makes it invisible to the optical microscope. The alignment of the actuator lithography with the graphene lithography is therefore impossible without going through the secondary step b). This consists of depositing nickel alignment marks on the wafer and then successively aligning the lithography of the graphene specimens and the nickel actuators with these marks. The nickel alignment marks are deposited using negative lithography. The thickness used is not important as long as the marks are visible (70nm is sufficient).

- In step c) extensively described in Section 3.2.2, the graphene film is transferred onto the wafer. The "fishing method" where the PMMA coated graphene sheet is "fished" out of the water with the wafer. This method is applicable in this case because there are no cavities in the wafer yet and there is no copper involved in the process.

- Step d) consists of positive lithography to pattern the graphene film into the desired beams, as explained in the section 3.2.3. Before applying the positive resist to the graphene, a 100 nm protective layer of PMMA is applied to the entire wafer, because the chemistry of the positive resist can damage the graphene. This also facilitates the removal of the resist after lithography. Once the resist has been patterned and developed, the graphene and its protective PMMA layer are removed using an oxygen plasma.

- Step e) is the actuator alignment and deposition. The actuator is made of nickel and is deposited by EBPVD, imperatively in Lift-Off mode as explained in the section 3.2.5. Negative photolithography is performed to pattern the actuators, as shown in the section 3.2.4. The typical thickness of the actuator is 100nm.

- The final step f) is the etching of a silicon layer under the test structures using XeF2, as explained in Section 3.2.6. All the stresses accumulated layer by layer during the fabrication of the test structure are finally released. A displacement is measurable when the balance of forces in the actuator and the specimen is established. The results of the release are explained in Section 4.

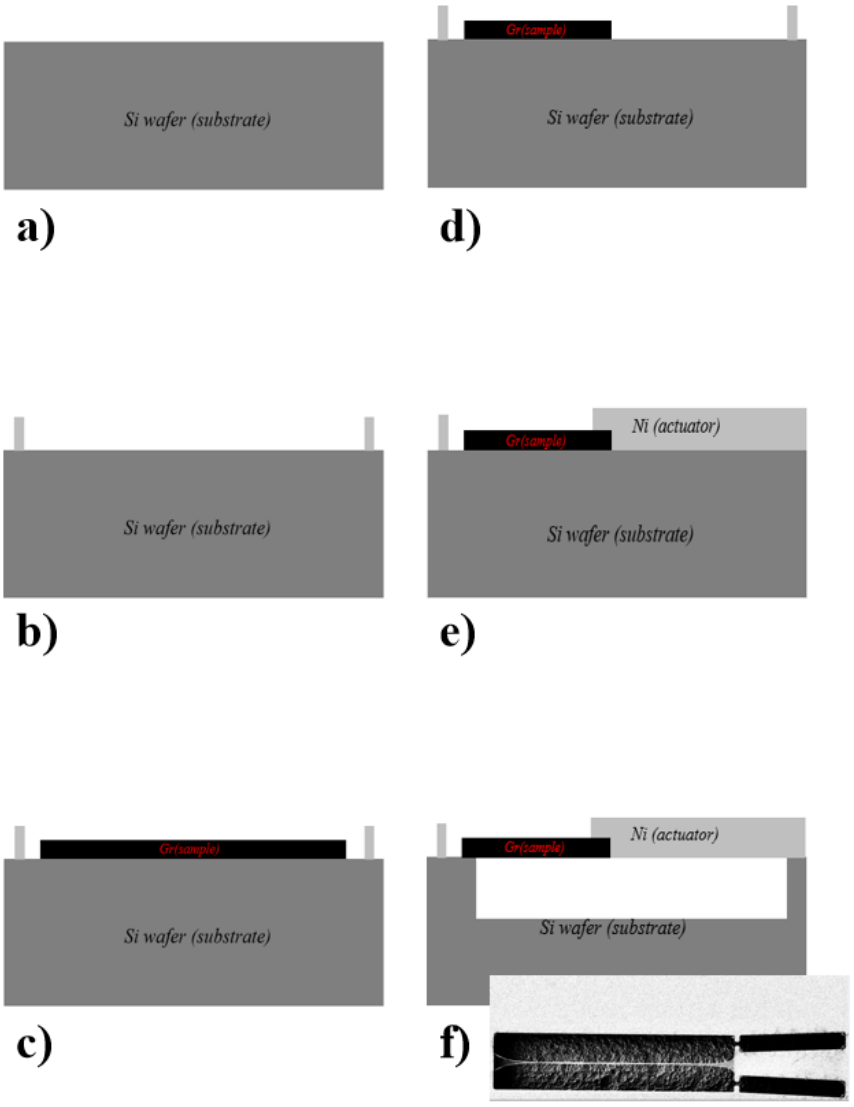

Figure 30: Process steps of lab-on-chip for graphene specimen: a) Standard cleaning, b) Nickel alignment marks deposition, c) Graphene transfer, d) Graphene positive lithography, e) Nickel actuator deposition and f) Release of the test structure, SEM image of a released structure of 100 nm graphene specimen.

3.4 Process LOC Cu+Gr

In this subsection, the process to manufacture a lab-on-chip for testing the superposition of copper and graphene is explained.

1. The standard cleaning is carried out in the wet benches in exactly the same way as for the LOC for graphene. Particular attention should be paid to dry the wafer before the following

steps, as copper oxidises on prolonged contact with water.

2. The wafer is put in the EBeam Vacotec for the physical vapour deposition of the copper layer, without forgetting the stoney wafer for the internal stress computation. As no negative lithography is performed on the copper, it can be deposited in rotating mode (see Section 3.2.5) in order to have a more homogeneous deposition. About 70 nm are deposited.

3. Graphene sheet is transferred onto the copper surface with the paper transfer technique (see Section 3.2.2). In this way, less water is trapped between the copper and the graphene. This prevents the copper to oxidize. The graphene sheet is about 3 cm by 3 cm in surface, meaning that there remains test structures with purely copper specimens on the wafer.

4. Then, the resist is coated using a Suss Gamma80 device, exposed with a Suss MA/BA6 Mask aligner and finally developed, as explained in Section 3.2.3. To etch the graphene and the protective layer PMMA, the same oxygen plasma is used, during 90 seconds at a power of 40 W. In order to etch the copper layer, the wafer is plunged in APS for 25 seconds and rinsed abundantly with water before going further with the next steps.

5. The deposition of the actuator goes in exactly the same way as for the test structures with graphene. The layer deposited in Lift-Off mode by the EBeam Vacotec is 100 nm thick.

6. The final step is the release of the structures in a SPTS Xactix e1 device. All the constraints build up in the test structures during the fabrication, layer by layer, can finally released, allowing the force balance to be established. The results of this release are explained in Section 4.

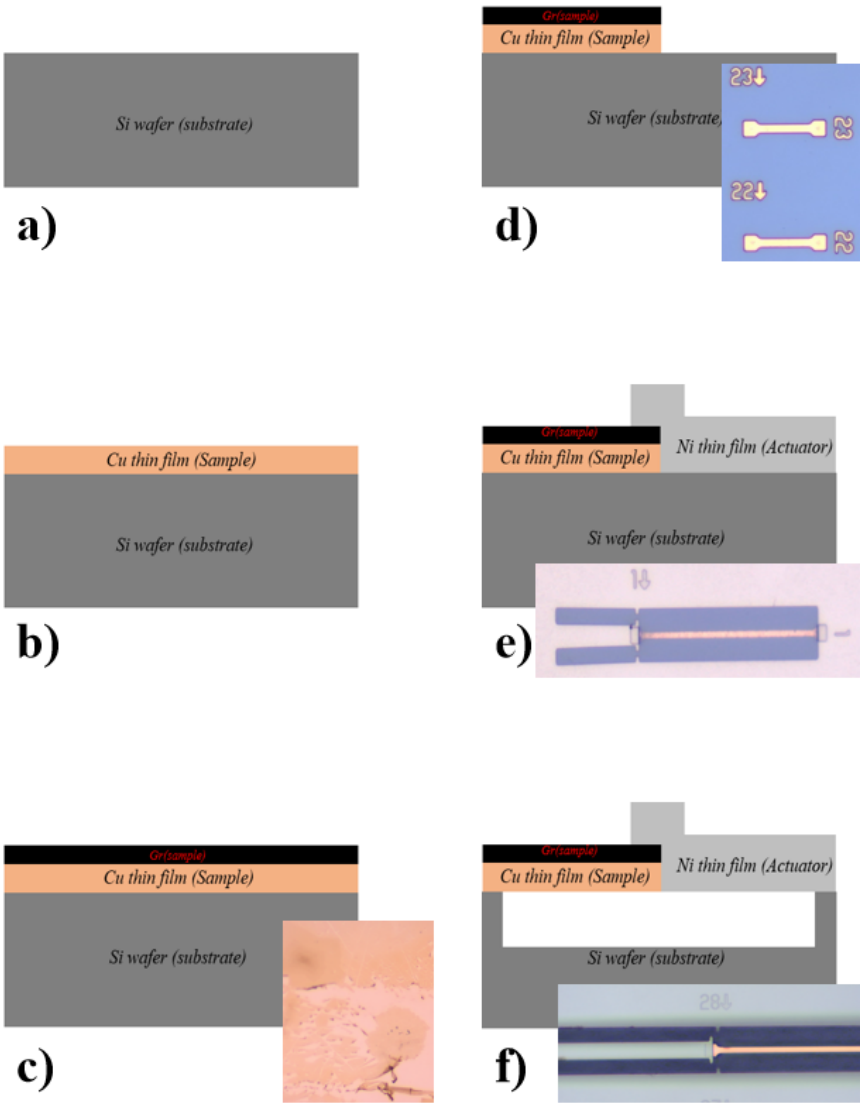

Figure 31: Process steps of lab-on-chip for graphene specimen: a) Standard cleaning, b) Cu deposition, c) Graphene transfer (optical picture of copper/graphene and copper alone), d) Graphene and copper positive lithography (optical picture of copper specimen after patterning), e) Nickel actuator deposition (optical picture of test structure B11 4 100 1) and f) Release of the test structure (optical picture of a released test structure.

3.5 Wafer layout

The wafers produced according to the process described in the previous subsections were patterned with the 2020 masks for the CuGr samples and the 2017 masks for the Gr samples. The LOC test structures studied in this work are almost identical in both mask generations. The layout of a 2020 wafer is as follows (see Figure 32): A wafer (a) contains 8 dice (b), lettered A to H. Each of these dice are containing all the test structures types necessary for the extraction of the stress strain curves of a material. Self-actuated structures, unloaded structures, structures for estimating the underetch during release, as well as the 'standard' test structures. When a release is performed, a whole die is released. In a die, the 'standard' test structures (d) are grouped in two groups of 30 in instances (c). Within an instance, the type of structure is the same, i.e. the width and length of the specimen do not vary. The length of the actuator varies from 50 microns to 1500 microns. A die contains 9 instances of specimens of 1.5, 2.5 and 4 microns width and 50, 100 and 400 microns length.

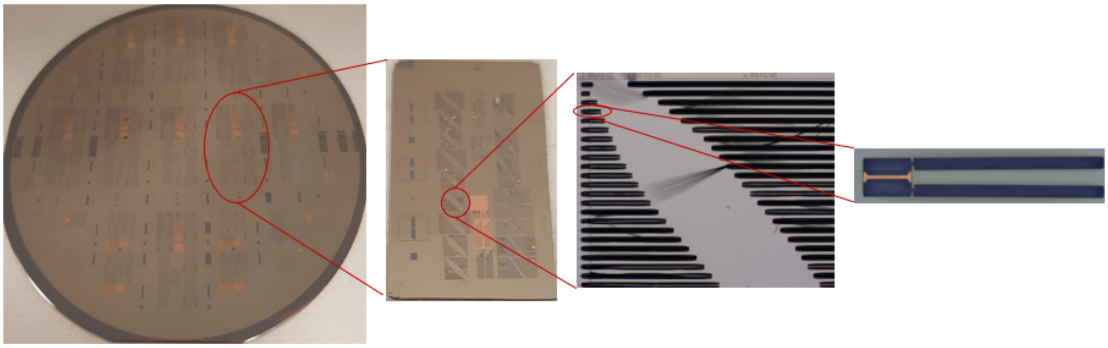

(a) Wafer level *(b) Die level* *(c) Instance level* *(d) Test structure level*

Figure 32: Layout of a 2020 LOC wafer

3.6 Main problems encountered for Cu+Gr LOC

The process described above is the result of extensive research and was not determined at first attempt. Different other ways of doing this were explored and eventually abandoned as less efficient. These are also worth mentioning.

3.6.1 Poor adhesion between copper and graphene

On all the samples produced, the adhesion between the graphene and the copper is poor. This is due to the fact that the graphene is transferred and not grown on the copper. The adhesion energy of transferred graphene on a copper thin film is estimated to $0.341\ J/m^2$ [45]. Delamination of the graphene layer is observed, as shown in Figure 33. Similarly, when the test structures are released, they are sometimes seen to be detached at the interface between the actuator and the specimen (see Figure 34). This problem is not seen on copper LOCs. The reason is probably that the nickel, which has a good adhesion with graphene (hence its use as an actuator on the graphene LOC), tears the graphene from the copper layer. The presence of the graphene in the specimen prevents the actuator from adhering to the specimen when the stress increases and therefore from reaching high strains.

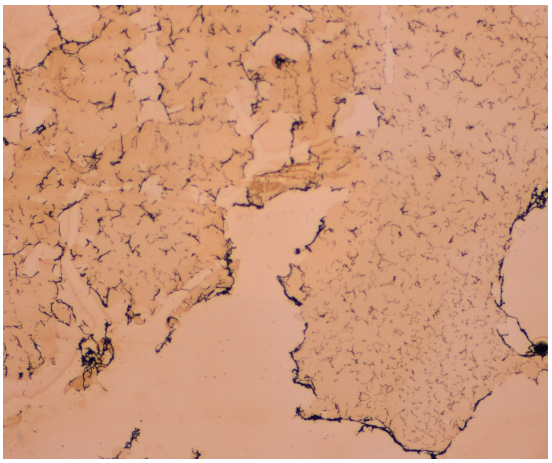

Figure 33: Delamination of transferred graphene on copper. Black lines are rolls of graphene

Figure 34: Adhesion issue between nickel actuator (on the left) and copper+graphene specimen (on the right)

3.6.2 Graphene under copper

The previous section describes a process in which copper is deposited prior to graphene transfer. The reverse has also been tried. By transferring the graphene first and then depositing the copper, several problems have arisen:

Firstly, putting the graphene under the copper makes it invisible to any analysis. So there is no way to prove the presence of graphene on the specimens or to check its quality. This problem was already known before starting the experiments, but if the quality of the samples obtained was excellent, one might have persisted, verifying the presence of graphene with, for example, the FIB.

Secondly, the adhesion between copper and graphene is not excellent. This poor adhesion is a problem during the nickel lift-off of the actuators. Indeed, when rinsing the wafers with acetone and water, the heavy copper layer tended to detach from the graphene, as shown in the Figure 35. When the graphene is on top of the copper, this was not too much a problem, because the thin and light layer of graphene does not tend to get carried away.

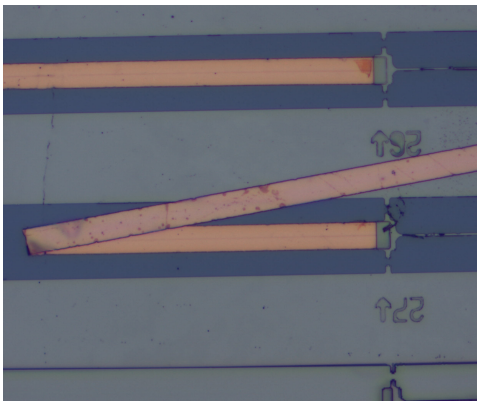

Figure 35: Unloaded structure of graphene+copper pulling on nickel with graphene under copper, before release. Copper has come out of plane during lift-off of nickel because of copper has a bad adhesion with the graphene deposited on the silicon substrate

3.6.3 Quality of the cursors

The cursors used for displacement measurements are part of the nickel actuators, so their quality is dependent on the resolution of the negative lithography of the actuators. The resolution of a lithography will be good if the exposure dose corresponds perfectly to the thickness of the coated resist on the wafer. On the photo-lithography machine used, the dose (expressed in mJ/cm^2) is controlled by the lamp power, for a constant exposure time. As the lamp is ageing, the exposure power varies slightly between exposures despite the calibrations, leading to sometimes questionable cursor qualities. Cursor resolution is critical to the accuracy of displacement measurements. Different cursor qualities were observed on the same wafer, allowing a measurement accuracy of around ± 60 nm and ± 20 nm for a bad and a good cursor resolution, respectively shown in Figure 36 and 37.

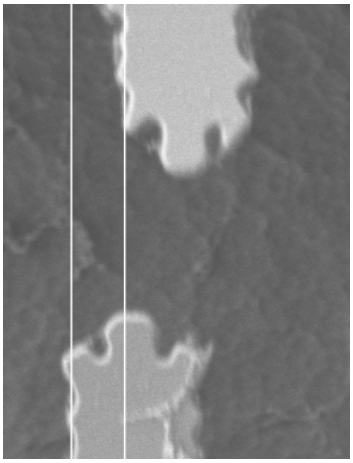

Figure 36: Nickel cursor with bad resolution (measurement error around 60 nm)

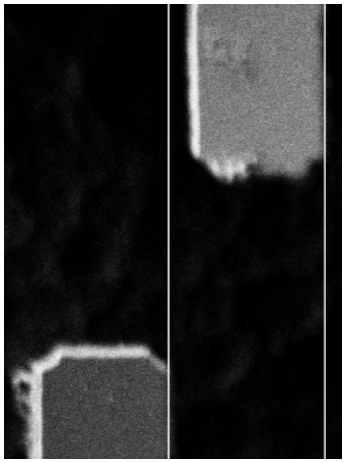

Figure 37: Nickel cursor with good resolution (measurement error around 20 nm)

3.6.4 Adhesion of the lift-off resist

As shown in Figure 38 (b), adhesion problem of the lift-off resist makes some of the CuGr test structures unusable. The problem is that the lift-off resist used to pattern the nickel actuators is too sticky, and is difficult to remove during lift-off. At the end of the lift-off, about 50% of the test structures remain covered with nickel.

Various solutions were tried to force the lift-off. The first was to leave the wafer in acetone at 60°C for a longer period of time. After 24 hours, the structures that were covered with nickel were still covered with nickel. 10 min of ultrasound (normally not used in the presence of graphene) did not improve the result.

To have a better lift-off, it is possible to keep the same resist but to increase the thickness coated. The edges through which the acetone enters the resist under the nickel would be larger, helping the resist to dissolve. However, changing the resist thickness would require readjusting the exposure dose for lithography, as the variable intensity ageing lamp would make this calibration complicated. Using another resist (AZ2020) which can be coated with a thicker layer gave an even worse result, where 90% of the test structures where still covered with nickel after lift-off.

In Figure 38, the darker areas indicated by (a) next to the actuator and the specimen of test structure n°9 is photoresist that has not left. On test structure n°8, it is the whole part of nickel above the specimen that stayed on place. Test structure n°7 is almost good but on the upper part of the actuator, resist is left, preventing it to actuate normally.

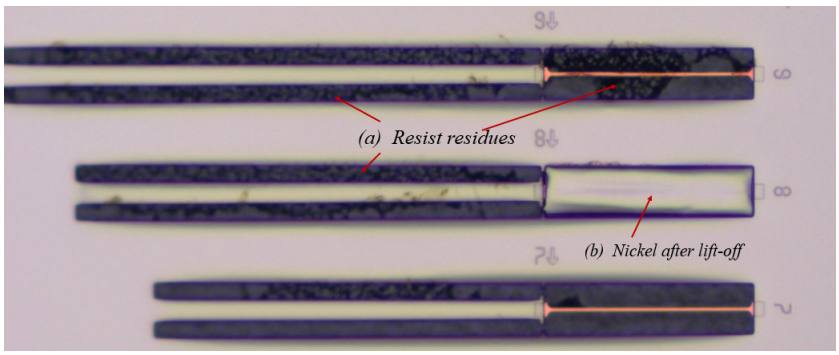

Figure 38: 100 μm long by 2.5 μm copper specimen actuated by nickel (a) shows lift-off resist residues and (b) shows nickel remaining after lift-off

3.6.5 Quality of the graphene

Check with Raman indicates a diminished quality of graphene after the release. As shown in Figure 39, the D peak that did not exist before the release is now as high as the 2D peak. The D peak, located below 1600 cm^{-1} is an indicator of the quality of the graphene, the higher it is, the more defected the graphene is. This result indicates that the order in the carbon atoms forming the graphene sheet has been deteriorated, by fluorination by the XeF_2 gas used for release. Fluorine atoms bind with the carbon constituting the graphene.

The effect on the graphene properties at high doses of XeF_2 (from 50 to 500 pulses) is a reduced modulus that increases with the fluorination percentage [46]. Graphene will also show increased electrical resistivity, up to 6 orders of magnitude more than pure graphene when fluorination saturation is reached (25%, for C_4F) [47]. For the application of release, the exposition of graphene to XeF_2 do not last long (around 15 pulses of 10 seconds), the fluorination will remain low and the pre-cited effects will not be strong. The fluorination percentage has the tendency to decrease from 50% to 80% in the week that follows the exposition [48].

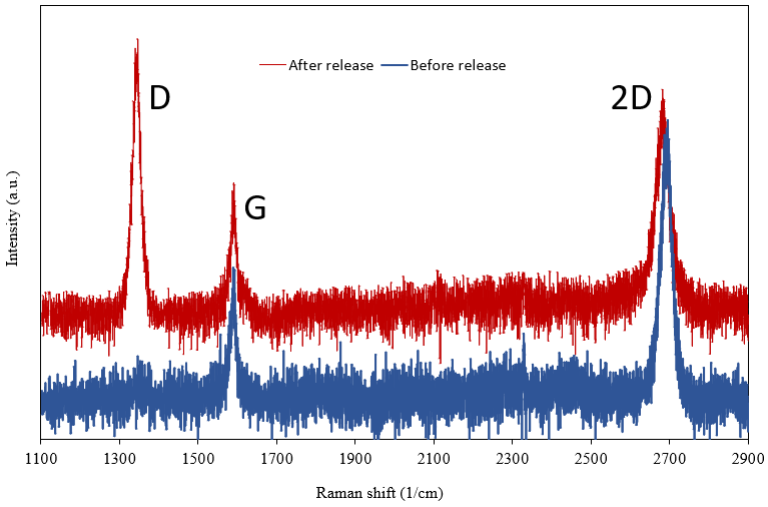

Figure 39: Comparison of the Raman spectrum of graphene before and after release.

4 Data analysis

4.1 Data extraction theory

The principle of the Lab On Chip is to provide actuation through an auxiliary material under high internal stress, integrated into the test structure. This auxiliary material, called the actuator, is attached to the specimen thanks to adhesion. The total is freed from the substrate by means of a gas, releasing the internal stresses of the actuator. The only measurable quantity resulting from this release is the displacement of the actuator-specimen interface. The distance u between the cursors indicates the to which extent the specimen has been extended (positive displacement) or retracted (negative displacement, in the case of poorly designed lab on chip). Negative displacements will not be considered.

The mechanical characterization of the specimen involves obtaining its stress-strain curve. This requires knowledge of both the strain and the force within the micro-machine. To calculate the force from the displacement of the cursors, it must be realized that the actuator also acts as a force sensor because its mechanical properties are known. The formula linking the force to the displacement of the actuator can be found in the following reasoning:

The total strain in the actuator is a description of its deformation, relative to its total length and is defined by 11. Approximation 12 leads to the definition of engineering strain, valid when the displacement u is small.

$$\epsilon_a = \epsilon_a^{mech} + \epsilon_a^{mis} = ln\left(\frac{L_{a0} - u}{L_{a0}}\right) \tag{11}$$

$$\epsilon_a \approx -\frac{u}{L_{a0}} \tag{12}$$

In which:

- The mechanical strain ϵ_a^{mech} is the elongation of the material due to a mechanical force applied to the ends of the beam, similar to a rubber band would be stretched with the fingers.
- The mismatch strain ϵ_a^{mis} can result from the difference in thermal expansion coefficient $\Delta\alpha_a$ between the actuator and the substrate and from the difference in deposition and measurement temperature ΔT_a in the following way: $\epsilon_a^{mis} = \Delta\alpha_a \Delta T_a$. In the case of a nickel actuator, internal stress is not of thermal origin but is induced by a difference in the lattice parameter between the substrate and the thin film [49].
- The displacement u is the difference in the cursor position before and after release. It is defined positive when the actuator shrinks and the specimen elongates.
- L_{a0} is the length of the actuator before the release.

In this equation, it is possible to develop certain terms by distinguishing the three states in which the actuator of a tensile test structure can be found (see Figure 40):

1. Not yet released, without any force applied. The displacement u then equals zero, the mismatch strain ϵ_a^{mis} is maximum. The mechanical strain ϵ_a^{mech} is naught as no force is applied at the ends of the actuator. The actuator is then at point 'one' on the force-displacement curve shown in Figure 41.

2. Totally released, without any force holding it back. The resulting displacement is the longest displacement achievable for that actuator length L_{a0}^{free}, and is called the free displacement u_{free}. Because no forces are applied at the ends of the actuator, the stress σ_a inside of it is naught. Consequently, $\epsilon_a^{mech} = \sigma_a / E_a = 0$. One can thus state that

$$\epsilon_a^{mis} = \epsilon_a = -\frac{u}{L_{a0}} \tag{13}$$

It is possible to calculate the mismatch for an entire wafer using the techniques described in Section 4.1.3, which allows the free displacement of the actuators of each test structure to be calculated, regardless of length. This situation is described by point 3 on the force-displacement curve (Figure 41).

3. Totally released, but with a load holding it back. The actuator is then in an intermediate position at point one and three. The actuator has been chosen for its linear behaviour when loaded, so the locus of the points reachable by the actuator in the stress-strain plane is the straight line connecting point one and three. Depending on the load applied, one is located somewhere on the red curve (Figure 41).

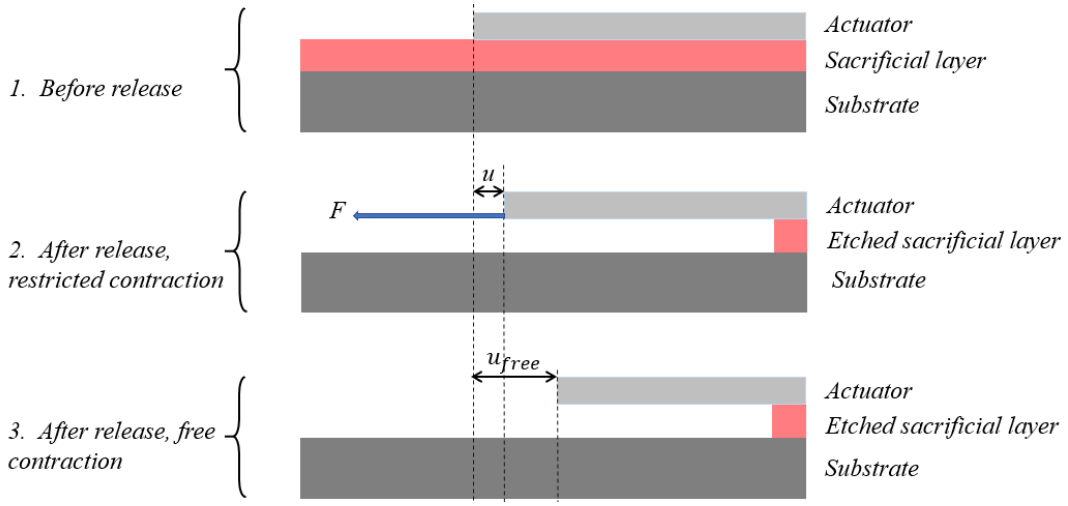

Figure 40: The three states of an actuator beam: 1. Before release, 2. After release, with restricted contraction and 3. After release, with free contraction

The force delivered by the actuator can be computed as:

$$F = S_a \sigma_a \tag{14}$$

$$= S_a E_a \epsilon_a^{mech} \tag{15}$$

$$= S_a E_a (\epsilon_a - \epsilon_a^{mis}) \tag{16}$$

in which S_a is the cross-sectional area of the actuator and E_a its Young's modulus. From Equations 12 and 13, one deduces the following expression of the force:

$$F = S_a E_a \left(\frac{u_{free}}{L_{a0}^{free}} - \frac{u}{L_{a0}} \right) = \frac{S_a E_a}{L_{a0}} \left(u_{free} - u \right) \tag{17}$$

In a tensile test structure, the force applied to the actuator is due to the presence of the specimen which prevents the actuator from retracting to its maximum. The forces in the actuator and the specimen are equal and opposite. As for the actuator but with an opposite displacement, the true mechanical strain in the specimen is obtained by the following formula:

$$\epsilon_s = \epsilon_s^{mech} + \epsilon_s^{mis} = ln\left(\frac{L_{s0}+u}{L_{s0}}\right) \tag{18}$$

$$\epsilon_s^{mech} = ln\left(\frac{L_{s0}+u}{L_{s0}}\right) - \epsilon_s^{mis} \tag{19}$$

The small displacement approximation cannot be reformulated here, however, because the specimen can sometimes undergo large displacements. As for the actuator, it is possible to calculate the mismatch by the methods described in Section 4.1.3. The mechanical strain of the specimen ϵ_s^{mech} can therefore be obtained by measuring the displacement u.

Since the force in the specimen is known, the calculation of the engineering stress is simply a matter of dividing the force by the cross-sectional area of the specimen, which gives:

$$\sigma = \frac{-F}{S} = -\frac{S_a E_a}{S}\left(\frac{u_{free}}{L_{a0}^{free}} - \frac{u}{L_{a0}}\right) = \frac{S_a E_a}{S L_{a0}}\left(u - u_{free}\right) \tag{20}$$

4.1.1 From engineering stress & strain to true stress & strain

In the previous subsection, the stress equation is given according to the engineering definition. Strain is sometimes simplified to its engineering definition, when it is referred to as the ratio of displacement to total length ($\epsilon^E = \frac{u}{L_0}$), in percent. Stress was referred to as the ratio of force to area ($\sigma^E = \frac{F}{S_0}$). This definition is intuitive but not very coherent, because it is not symmetrical. Indeed, an elongation of a factor of 2 gives an engineering strain $\epsilon^E = \frac{2L_0 - L_0}{L_0} = 1$, but a compression of a factor of 2 does not give an engineering strain of -1 but of $\epsilon^E = \frac{L_0/2 - L_0}{L_0} = -\frac{1}{2}$. To be more accurate, it is preferable to speak in true strain values, defined as follows:

$$\epsilon = ln(\frac{L}{L_0}) \tag{21}$$

With this new definition of strain, an elongation by a factor of 2 gives a true strain of 0.69 and a compression by a factor of 2 gives a value of -0.69, which is now symmetrical. The link to go from the engineering definition to the true definition is the following:

$$\epsilon = ln(1+\epsilon^E) \tag{22}$$

$$\epsilon^E + 1 = e^{\epsilon} \tag{23}$$

$$\sigma = \sigma^E(1+\epsilon^E) \tag{24}$$

The true stress is obtained by starting from Equation 24 and filling in the engineering stress 20 and Expression 23. The true stress is given by:

$$\sigma = \sigma^E \cdot \qquad (1+\epsilon^E) \tag{25}$$

$$= \frac{F}{S_0} \cdot \qquad (1+\epsilon^E) \tag{26}$$

$$= \frac{S_a E_a}{S}\left(\epsilon_{act}^{mis} + ln(\frac{L_{a0}-u}{L_{a0}})\right) \cdot \qquad e^{\epsilon} \tag{27}$$

4.1.2 Physical interpretation of the data extraction

The physical interpretation of Figure 41 a) is as follows: Curve 'Actuator L1' is the force-displacement curve of the first actuator with length L1. It is a linear curve, because the actuator material was chosen for its linearity in the elastic range. This curve is known, for a given displacement it is possible to calculate the force. The other curves are those of other actuators of decreasing length. The blue curve is the unique force-displacement curve of the specimen. This curve is the one sought.

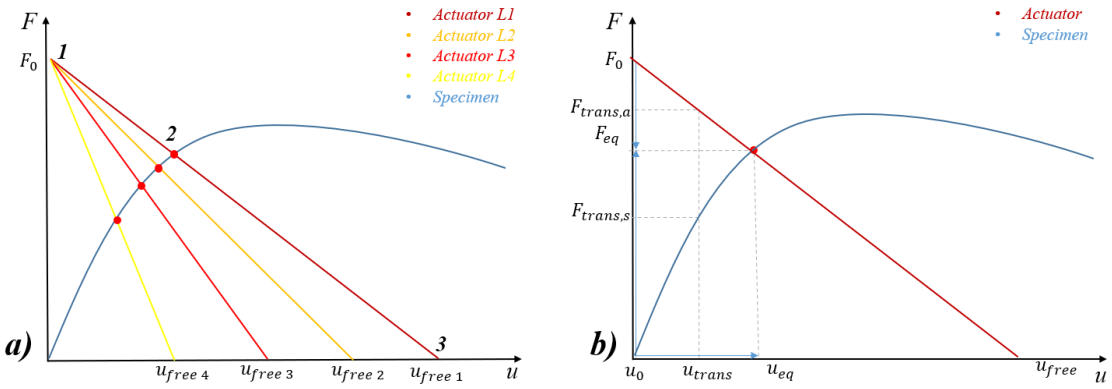

Figure 41: a) The force displacement curve for 4 length of actuator L1>L2>L3>L4 and one specimen material. b) The evolution of the force and displacement during the release of a test structure. The three different states for actuator L1 are numbered on the figures.

To determine a single red point of the specimen's curve, one micro-machine is needed. When the latter is not yet released, it is in the displacement state $u_0 = 0$. All the mismatch strain accumulated during the process is in the actuator, and the specimen is not yet strained. When the sacrificial layer is etched, the mismatch strain in the actuator is released, and is partially transformed into mechanical strain, pulling on the specimen. The total force in the actuator then decreases linearly as it retracts. The specimen, initially at zero displacement and zero force, sees its state shift to the right and upwards, as the force imposed on it grows and its displacement increases. This transitory state is described by Figure 41 b). At displacement u_{trans}, the force in the actuator is larger than the force in the specimen ($F_{trans,a} > F_{trans,s}$). When the forces within the test structure have balanced, its state is known to be the intersection of the known actuator curve and the unknown specimen curve. The displacement of the sliders can then be measured, allowing the force to be found from the actuator curve and finally a point of the force-displacement curve of the specimen can be placed. By repeating this process for different actuator lengths, the entire force-displacement curve of the specimen can be found.

4.1.3 Mismatch strain computation

In order to calculate the position of a point on the force-displacement curve of the specimen, it is necessary to know the displacement u and the displacement u_{free} that the actuator would have made if it was not attached to the specimen. The measurement of u is done after the tensile test structure is released. But measuring the u_{free} displacement for each actuator individually would require a lot of time and space on the wafer (each test structure would have to be split into two, one loaded, the other not). Furthermore, releasing an actuator that is not connected to a stub will often involve it

going out of plane or breaking. It will be simpler to calculate the u_{free} for all actuator sizes, which is simply the length of the actuator before release multiplied by the mismatch:

$$u_{free} = L_{a0} \cdot \epsilon_a^{mis} \tag{28}$$

The mismatch itself is calculated for a whole sample thanks to some structures especially dedicated to this.There are several types, such as rotary sensor, free lever or self-actuated structures. The latter are the ones used in the samples studied in this work. Self-actuated structures are lab-on-chip test structures, made of a material that draws on the same material. It is therefore composed either entirely of the material of the actuator or entirely of the material of the specimen. In the case of tensile stress, the side with the larger width overrides the thinner one, allowing a displacement to be measured. Similarly to Equation 17, the force within the test structure will be given by:

$$F = S_a E \left(\epsilon^{mis} - \frac{u}{L_{a0}} \right) \tag{29}$$

$$= SE \left(ln \left(\frac{L_0 + u}{L_0} \right) - \epsilon^{mis} \right) \tag{30}$$

where Equations 29 and 30 are the equations from the actuator's and specimen's point of view respectively. By rearranging the terms, the following relationship is obtained for the calculation of the mismatch:

$$\epsilon_{mis} = \frac{Sln \left(\frac{L_0+u}{L_0} \right) - S_a \frac{-u}{L_{a0}}}{S - S_a} \tag{31}$$

4.1.4 Underetch and dogbone shape

To refine the calculation of stress and strain within the specimen, Ghidelli *et al.*[50] have developed a way to take into account the influence of the underetch and dogbone shape of the specimens on the measured displacements. The underetch is the distance that has been etched under the actuator and specimen layers. It is therefore expressed in nanometres. The dogbone shape is the enlargement of the specimen beam, which is not taken in the length of the specimen but still elongates a bit and contributes to the measured displacement. Those are shown in Figure 42. On that sample the underetch is visible because it has been half-released for 8 months, during that time the etched parts of the nickel could age.

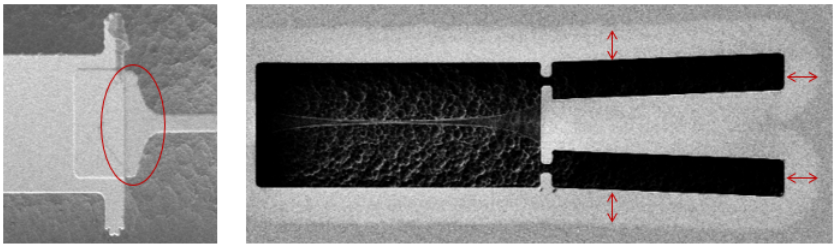

(a) Dogbone shape *(b) Underetch*

Figure 42: (a) dogbone shape of a copper graphene specimen and (b) underetch of a graphene-only test structure actuated by nickel

It influences the length of the actuator by $L_{a0} = L_{a0}^{name} + L_{ue}$. The free displacement becomes $u_{free} = u_{free}^{name} + \epsilon_a^{mis} L_{ue}$.
The gauge length of the specimen is increased by the underetch length and the dogbone shape length ($l_{tot} = l_{ue} + l_{gauge} + l_{db}$). The underetch length and the dogbone shape length also lengthen a little under the force of the actuator and represent a part of the measured displacement. However, one does not want to take these displacements into account. We therefore subtract them from the measured displacement, in order to find only the displacement u of the gauge:

$$u = u_{measure} - u_{db} - u_{ue} \tag{32}$$

in which the displacement due to the dogbone u_{db} and the displacement due to the underetching u_{ue} are obtained as:

$$u_{db} = U_{meas} \frac{w}{w_{db}^{eff}} \frac{l_{db}}{l_{tot}} \tag{33}$$

$$u_{ue} = U_{meas} \frac{w}{w_{ue}^{eff}} \frac{l_{ue}}{l_{tot}} \tag{34}$$

w, w_{db}^{eff} and w_{ue}^{eff} are the specimen width, the effective dogbone width and the effective underetching width. In this work, the width ratios are taken equal to $\frac{w}{w_{db}^{eff}} = \frac{w}{w_{ue}^{eff}} = \alpha = 0.3$ One should note that for the graphene-only specimens, there is no dogbone shape, the correction related to it should not be done.

4.2 Error propagation

Displacement measurements are made with the Zeiss Gemini Ultra-55 scanning electron microscope (SEM) using the in-lens detector. For each test-structure, there are two pairs of cursors which are each measured once at each side, thus leading to four measurements per test-structure (see Figure 43). Measures are performed with a 10k magnification. With the formulae detailed in the previous sections, the measures are converted into useful data, such as the stress-strain curve.

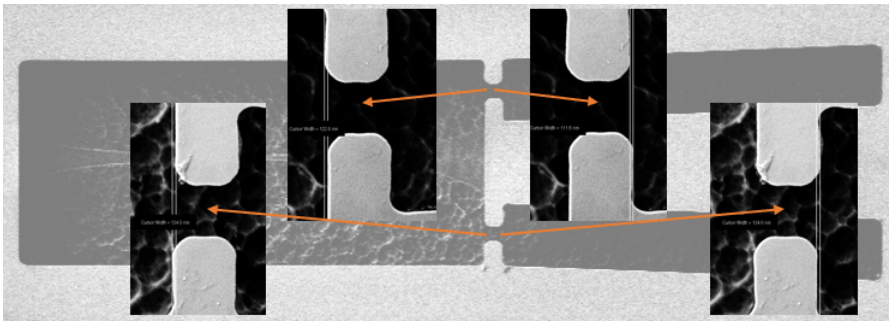

Figure 43: 4 measurements per test structure, performed in 10k magnification

4.2.1 Propagation of the measurement error

The accuracy of the measurements depends mainly on the quality of the cursors and can vary from 20 nm for the most accurate measurements to 60-70 nm for poor cursors. These measurement errors

have been integrated in the computation of the stress-strain curves. The error on the stress and on the strain increases linearly with the measurement error as shown on Figure 44.

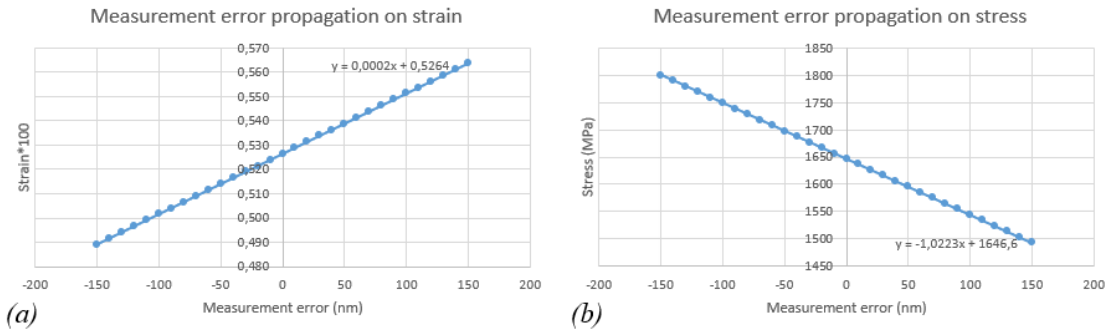

Figure 44: (a) Strain and (b) stress error in function of measurement error, for the Cu test-structure B11 4 400 23 (specimen of $400\ \mu m$ long by $4\ \mu m$ wide, and an actuator of $950\ \mu m$)

The influence of a certain measurement error Δu will influence the stress and strain differently depending on the length of the specimen and actuator of the test structure considered.

- The longer the specimen, the less the influence of the measurement error on the strain error. This is due to the fact that when a specimen is short, the displacements measured are small. The same error Δu will proportionally influence more the measurement of a small displacement than a large displacement. With the same measurement error Δu, the strain error on a $50\ \mu m$ specimen is twice the error on a $100\ \mu m$ specimen (see Figure 45, (a)).
- The longer the actuator beam, the less the influence of the measurement error on the stress error (Figure 45, (b)). The reason is that the slope of the stress strain line of a shorter actuator is steeper. When computing the stress with a measurement containing a certain error Δu, it will be more ($\Delta\sigma_2$) or less ($\Delta\sigma_1$) amplified if the slope of the actuator is respectively steeper or shallower. This is illustrated by Figure 46.

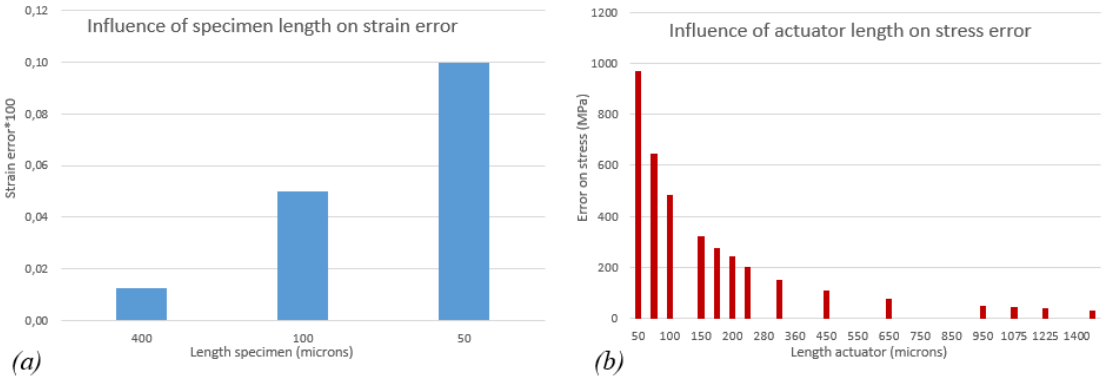

Figure 45: (a) shows the influence of the length of the specimen L_{s0} on the strain error and (b) shows the influence of the length of the actuator L_{a0} on the strain error for copper specimen of $4\,\mu m$ width by 1.5, 2.5 and $4\ \mu m$, with an 50 nm error on the measurement

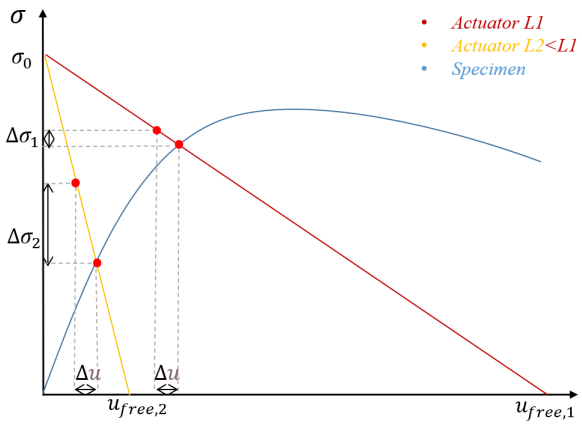

Figure 46: Stress error dependence on the length of the actuator

The consequences of these considerations are that the stress measurements of the shortest actuators are not usable because they are too uncertain (usually the first 7-8 structures). With conventional LOC structures, it is difficult to plot precise stress-strain dots in the elastic deformation regime, close to the origin of the stress-strain plane. Taking short actuators would give an inaccurate measure of stress. Decreasing the ordinate of the curve σ_0 by decreasing the thickness of the actuator would allow to use longer actuators again, but this can not be done indefinitely for structural reasons.

4.2.2 Propagation of the mismatch error

As indicated in the formulas 19 and 27, the mismatch of the specimen ϵ_s^{mis} only influences the strain, and the mismatch of the actuator ϵ_a^{mis} only the stress. In both cases, the relationship between mismatch and stress or strain is linear, as shown in Figure 47. It is also noticeable that the ϵ_s^{mis} has little influence on the strain, the stress-strain curve shifts horizontally by ± 0.0006 while the ϵ_s^{mis} equals 0.0003, 0.0009 and 0.0015 (multiplication by 3, then by 1.66). ϵ_a^{mis} on the other hand, when increasing from 0.0030 to 0.0035 to 0.0040 (multiplication by 1.16, then by and 1.14), implies large vertical displacements of the stress-strain curve ($\pm 500\ MPa$).

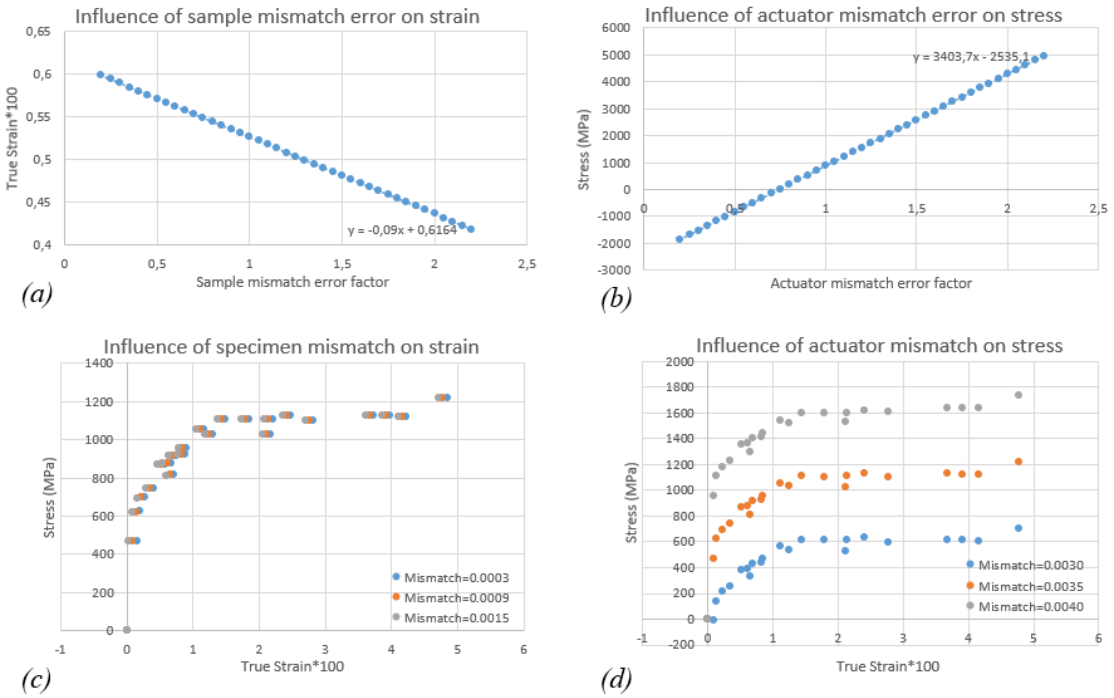

Figure 47: (a) Strain in function of the sample mismatch error factor and (b) stress in function of the actuator mismatch error, for the Cu test-structure B11 4 400 23 (specimen of $400\ \mu\mathrm{m}$ long by $4\ \mu\mathrm{m}$ wide, and an actuator of $950\ \mu\mathrm{m}$). (c) and (d) are the stress-strain curves of 4 micron wide copper specimen, where respectively the specimen mismatch and the actuator mismatch were played with.

4.2.3 Propagation of the width and thickness error

The width and thickness of both specimen and actuator influence the stress in a purely proportional way. An error of 10% on one of the two will give an error of 10% on the stress. They do not influence the strain.

4.3 Results for Graphene LOC

Interpreting the results of a LOC on graphene is tricky, because the thickness of the graphene layer ($\pm 0.3\ nm$) is two orders of magnitude smaller than that of the actuator $\pm 70\ nm$. Doing a tensile test on graphene could therefore amount to pulling on nothing at all, and one would then measure displacements similar to that of free beams, whether or not graphene is present.

If this hypothesis is correct, the displacement of a graphene specimen should systematically be equal to the U_{free} displacement of its actuator. This displacement should not depend on the width or length of the graphene being pulled on, but only on the length of the actuator (and thus on the structure number).

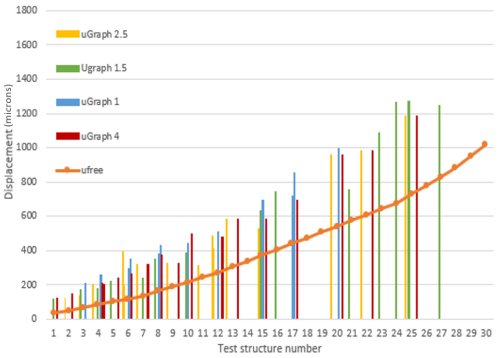

Figure 48: $1\ \mu m$, $1.5\ \mu m$, $2.5\ \mu m$ and $4\ \mu m$ wide graphene specimen displacement compared to their U_{free}

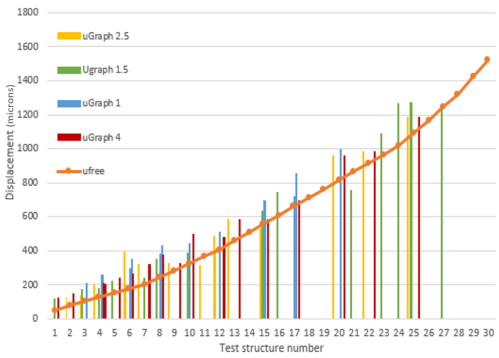

Figure 49: Same measures as Fig. 48 compared to the adapted free displacement $U_{free} \cdot 1.5$

In Figure 48, all the measurements made in the 24 hours following the release of a graphene sample have been grouped by structure number. The sample had been partially released (7 pulses of $\sim 300\ Pa$) in August 2020, and fully released in April 2021. The thickness of the nickel actuator is 70 nm. The orange line is the U_{free} displacement for each structure number. U_{free} is computed with Equation 28 ($U_{free} = L_{a0}\epsilon_a^{mis}$), where ϵ_a^{mis} was obtained with the measure of displacement of the auto-actuated structures with Equation 31. U_{free} should be systematically greater than the displacement of the specimens but this is not the case. The only way to explain a U_{free} smaller than all the specimen displacements is an erroneous mismatch value, the actuator length L_{a0} being a known manufacturing parameter, and the measured displacements being correct to within $20\ nm$. Empirically, it can be seen that the mismatch must be multiplied by about 1.5 to obtain a U_{free} curve similar to that of the measured specimens, as shown in Figure 49. This difference is explained by the fact that auto-actuated structures are designed for elastic deformation only. But, for nickel auto-actuated structures, plasticity is reached in the specimen part. It can be seen in Figure 51 (b) that the mismatch decreases as the actuator length increases, whereas it should be constant for any test structure. This is due to the fact that the plastic regime in the specimen is more strongly initiated for longer actuators. The more plasticity, the smaller the (erroneous) mismatch obtained. Auto-actuated structures thus underestimate the mismatch because of plasticity. This has been verified for other samples (a sample that was produced and released in August 2020 and a sample produced and released in March-April 2021, both of lower quality and less measured).

In Figure 49, it can be seen that there is no pattern in the displacements obtained for each type of specimen. The specimens that can withstand the greatest force (the 4 microns wide) are not especially the least elongated, and the specimens that can withstand the smallest force (1.5 microns wide) are not especially the most elongated. The displacements measured looks randomly distributed around the $U_{Free} \cdot 1.5$ curve. These results are in contradiction with the measurements of a set of 50 micron long by 1 micron wide structures produced and released in March-April. According to the hypotheses that graphene do not contribute to the displacement, the measured displacements should match the $U_{Free} \cdot 1.5$ curve. For this sample, the displacement is clearly decreasing with regard to the free displacement when the actuator length increases, as shown in Figure 50. To explain this, the difference between the displacement with and without graphene is computed, in the same way as in Subsection 4.5. An instance with the same parameters as the one plotted in Figure

50 is used ($L_{0,sample} = 50\ \mu m$, $W_{0,sample} = 1\ \mu m$, $\epsilon_{act}^{mis} = 0.13 \cdot 1.5 = 1.195$, $t_{act} = 70\ nm$, and $E_{Gr} = 1000\ GPa$, $E_{Ni} = 240\ GPa$ [51][52; 53]). The computations shows that graphene makes almost no difference on the measured displacement (<1 nm) for structure 1. For structure 30, a difference of 130 nm is computed. It shows that the hypothesis is not valid when the length of the actuator increases. Graphene can be responsible for displacement variations. This is not visible on the sample released in August because not enough measures could be realized on the same instances.

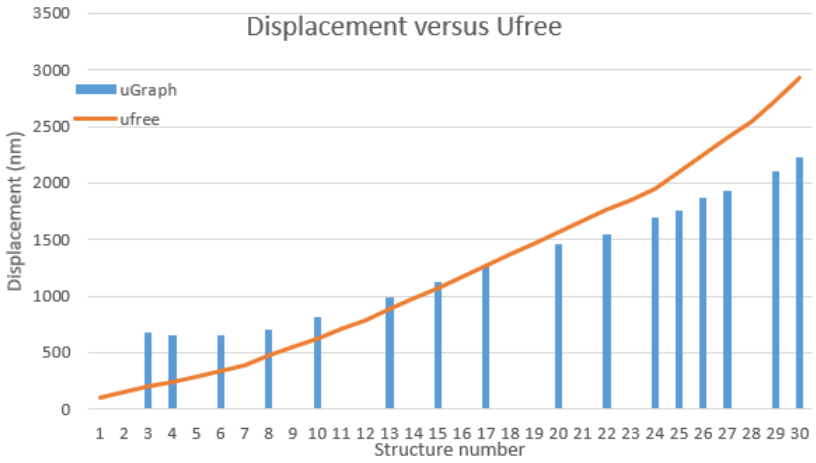

Figure 50: Displacement measurements of 50 μm long, 1 μm width graphene specimens produced and released in March-April 2021, compared with $U_{Free} \cdot 1.5$

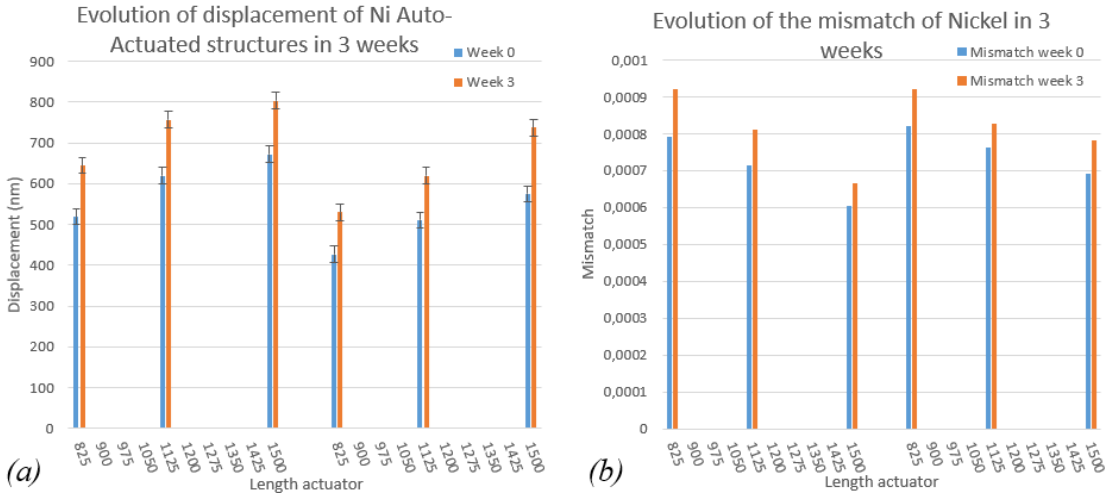

Figure 51: (a) Displacement in the nickel autoactuated structures, first measurement (week 0, blue) and second measurement after three weeks (week 3, orange). Error bars for a measurement error of 20 nm have been added. (b) Mismatch obtained with Equation 31 from the displacements from (a).

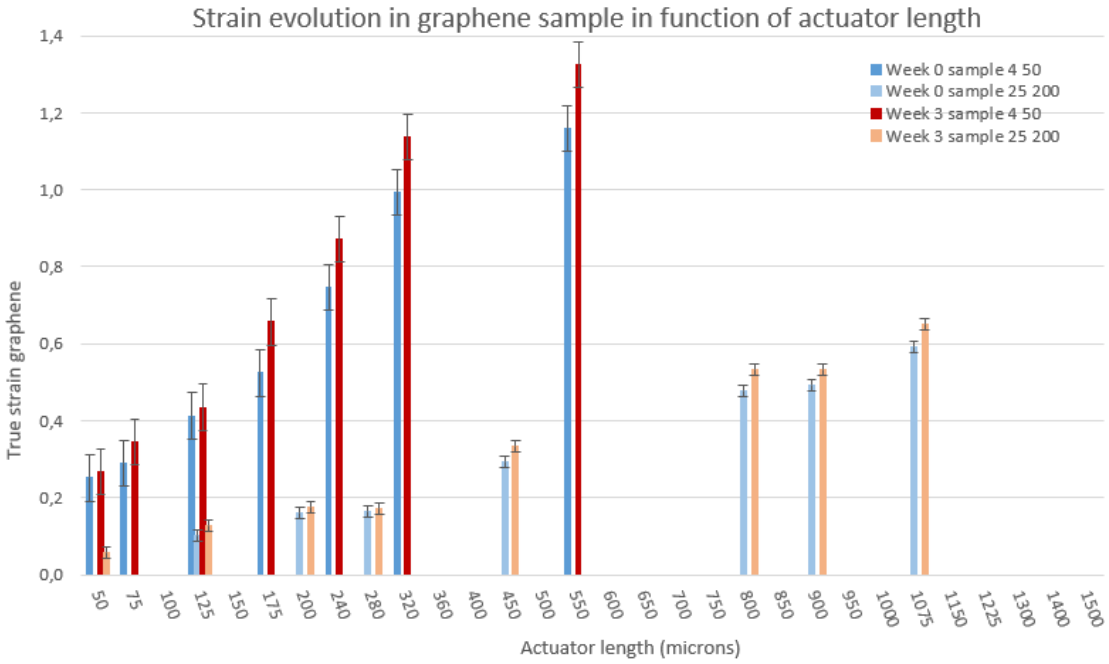

Figure 52: Strain in function of length actuator, for first measurement (week 0, blue) and second measurement after three weeks (week 3, red)

Testing graphene with LOC makes a second observation possible. The sample used for the above considerations was re-measured three weeks after its release. Figure 52 shows the evolution of the strain within the 4 micron wide graphene specimens. It can be seen that the strain has increased overall in each structure by $\pm 23\%$. This is not due to relaxation in the internal stresses of the specimen because graphene is so thin that it should not influence the measured displacement, regardless of its length, width and stress state. The increase in strain is due to evolution of the stress state of the nickel actuator. This finding is confirmed by measurements of self-actuated nickel structures (Figure 51 (a), for which the displacement also increased.

- A first explanation for the change in the stress state of nickel is reverse creep. Nickel could show viscoplastic behaviour, for which the contraction continues at constant rate for long time after release. This phenomenon, driven by heterogeneity of internal stresses of nickel is known as kinematic hardening [54]. It is known that nickel creeps [55], but further study should be performed to quantify the creep rate. The measured evolution is too high to be explained only by kinematic hardening, a second factor is increasing this large evolution.

- The second factor to the large evolution measured is that this sample received 7 pulses of XeF_2 in August, which was not enough to release it fully. Obviously, no displacements were observed. The release was finished in April. During 8 months, only the edges of the actuator (Figure 53 (a)) were released. The equibiaxial stress state in the released part of the actuator can evolve in a longitudinal uniaxial stress, because of transverse stress elastic unloading. It

is then multiplied by $1 - \nu = 0.7$, where $\nu = 0.3$ is the Poisson ratio of nickel. Relaxation in the released part of the actuator had time to weaken the uniaxial longitudinal stress. Once released, the elastic unloading of the actuator provided the displacement measured at the first time. During the three weeks that followed, the freshly released part of the actuator (Figure 53 (b)) that still contained some stress could actuate further at slower rate, inhibited by the relaxed parts of the actuator. The displacement measured for the second time are larger because of the elastic recovery of the central part of the actuator.

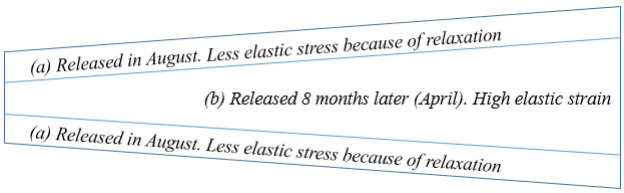

Figure 53: Schematic of a nickel actuator released in two stages(a) First released part of the actuator, subject of relaxation for 8 months. (b) Central part of actuator, released just before the first measurement.

The maximum true strain measured on a graphene specimen was 0.0435, obtained for test structure B11 1 50 30 (1 microns width, 50 microns length and an actuator of 1500 microns length, produced and released in March-April 2021). The specimen is shown in Figure 54. The measurement of the stress makes no sense with graphene specimen, as the thickness of graphene is not well defined. The measurement of the (very weak) force in the specimen can not be accurate, because the mismatch of the actuator is not known with precision.

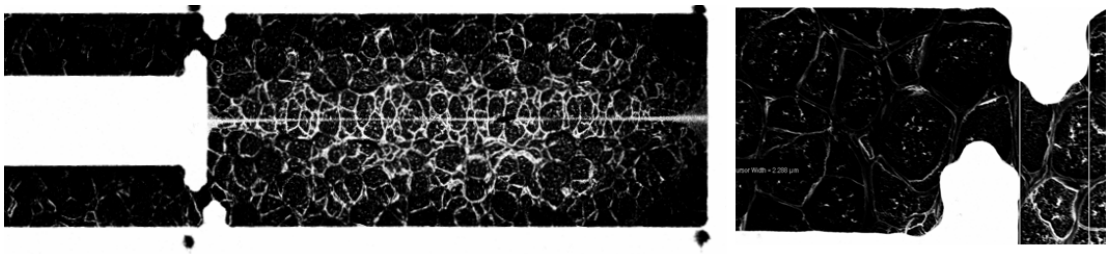

(a) Graphene specimen B11 1 50 30 *(b) Measured displacement: 2288 nm*

Figure 54: (a) Graphene test structure B11 1 50 30 SEM image, (b) Displacement measure of 2288 nm in x10k magnification

From the measures made on graphene LOC, it can be concluded that the measure of the actuator mismatch with auto-actuated structures is not reliable when the actuator is made of nickel because of plasticity. This deduction is also valid for the copper and copper/graphene samples. Then, one can state that nickel creeps, but at a yet unknown rate.

4.4 Results for Copper LOC

Copper samples are obtained from the same wafer as copper/graphene samples studied in Section 4.6, from the parts of the wafer where no graphene was transferred. The analysis of copper specimens is useful to compare with copper/graphene specimens, especially if those are from the same wafer. The parameters of the wafer manufactured are the following: copper thickness $70\ nm$, nickel thickness $105\ nm$, first measurement in 24 hours after release.

The mismatch of the copper specimen is computed with the specimen dedicated auto-actuated structures. A value of 0.000914 is obtained. The mismatch of the nickel actuator is computed with three methods to compare them. The first method is the auto-actuated structures of the sample, with Equation 31. A value of 0.0045 is obtained, but auto-actuated structures do not give reliable results, as explained in Subsection 4.3. The second method is the measure of in plane freestanding beams for which the specimen broke. The mismatch is then simply equal to the measured displacement divided by the length of the actuator. Three valid free beams were found on the copper sample, giving a value of mismatch of 0.0040 (this value is confirmed by five free beams of the copper/graphene part of the wafer). The third method is curvature measurement (see Section 2.2.2). The obtained internal stress in the nickel thin film is 1017 MPa, which gives a mismatch of

$$\epsilon_{act}^{mis} = \sigma_f(1-\nu)/E_f = 0.00147 \tag{35}$$

[56] where the Young's Modulus $E_f = 214GPa$ as found in literature [52; 53]. The three methods lead to different results. In this case, the most reliable measures are the free beams and the value used is 0.0040.

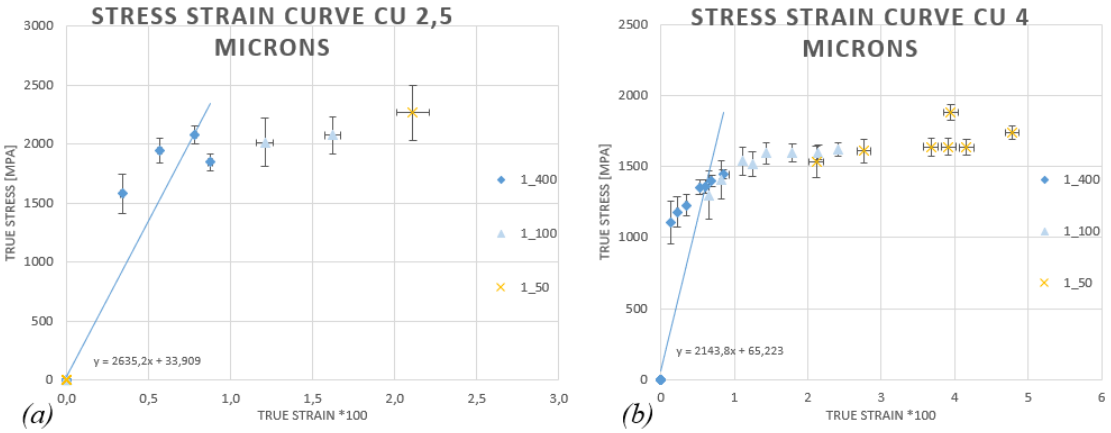

Figure 55: Stress strain curves of (a) $2.5\ \mu m$ and (b) $4\ \mu m$ wide copper sample, with a mismatch of 0.0040 and a measurement error of 50 nm

Using a mismatch of 0.0009 for the copper and of 0.0040 for the nickel, the stress-strain curve obtained for the 4 micron wide copper specimen is shown in Figure 55. The two slopes are the linear regressions of the 400 long specimen stress strain state. The Young's modulus [GPa] of copper can be obtained by dividing the slope by 10 to compensate for the units of the graph (strain is multiplied by 100, stress is in MPa instead of GPa), giving the following results. The ultimate tensile stress is taken as the highest stress value of the stress-strain curve:

$$E_{2.5} = 263.5\,GPa \quad (36) \qquad \sigma_{2.5}^{max} = 2269\,MPa \quad (38)$$

$$E_4 = 214.3\,GPa \quad (37) \qquad \sigma_4^{max} = 1884\,MPa \quad (39)$$

The Young's Modulus of copper should normally have values of 100-150GPa [57]. Values of ultimate tensile stress of copper should be in the range of 570 MPa [54]. Both the Young's Modulus and ultimate tensile stress are too high.

Too high stress measurement can be due to too high actuator mismatch estimation. A small change in the mismatch value leads to high stress changes, as seen in Subsection 4.2.2. Mismatch values obtained with auto-actuated structures are not reliable. With an actuator mismatch of $\epsilon_{act}^{mis} = 0.0035$, acceptable values of stress and Young's Modulus are obtained:

$$E_{2.5} = 136\,GPa \quad (40) \qquad \sigma_{2.5}^{max} = 1334\,MPa \quad (42)$$

$$E_4 = 138\,GPa \quad (41) \qquad \sigma_4^{max} = 957\,MPa \quad (43)$$

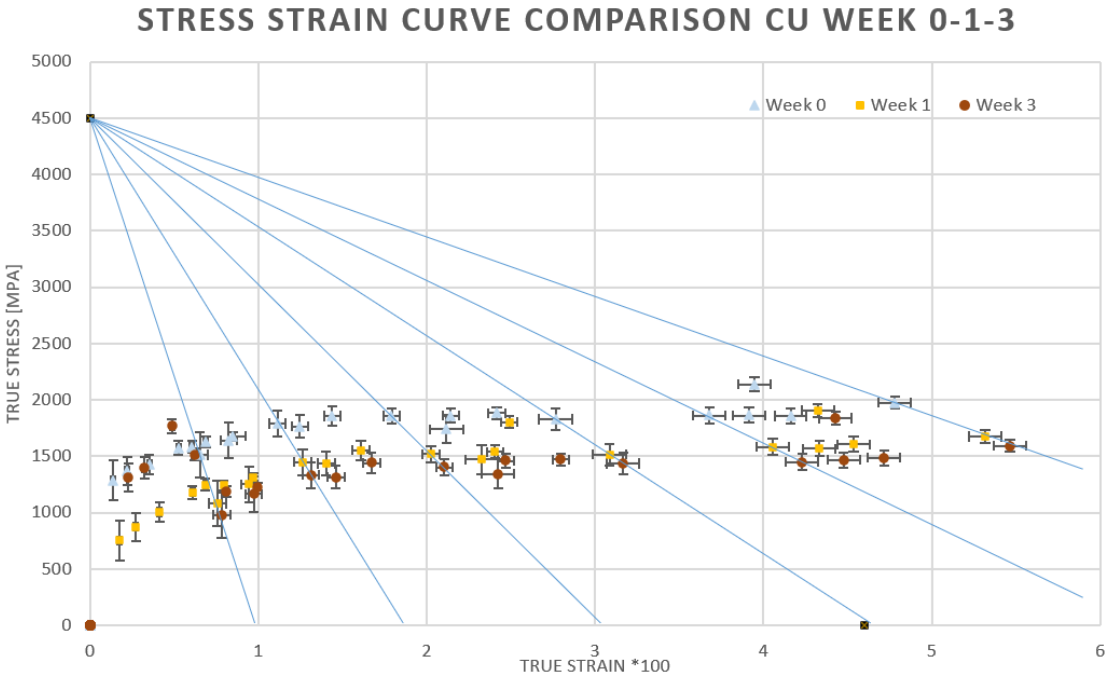

Figure 56: Evolution of 4 microns wide copper specimen stress strain curve

Figure 56 shows the time evolution of the 4 microns wide copper specimen stress-strain curve. Cu 1 is the first measurement, directly after release, Cu 2 one week after release and Cu 3 three weeks after release. The lines are the stress strain curves of some actuators with different lengths. One sees that over three weeks, the stress-strain state of one structure evolves with one actuators lines. This is logic because the stress-strain state of the structures are computed thanks to the known actuator stress strain curve. Over three weeks, the strain in the structures increased by about 14% leading

to a global decrease in stress of about $350\,MPa$. The maximal true strain measured is 0.0546 (for structure n°25 of 4 μm width an 50 μm length). It is interesting to note that the creep behaviour along one line seems to slow down with time, as is be expected. There is a large gap between the first and the second measurement (one week between the two). The gap between the second and the third measurement is about 2.5 times smaller than the first gap, while two weeks separates them. The creep rate seems to decrease with time, which is an intuitive result.

This important time dependent behaviour is due to reverse creep in the nickel actuator and relaxation of the copper specimen. It is difficult to quantify the time evolution of copper, as the contribution of the creep of nickel is unknown as well.

4.5 Results expectations for Copper+Graphene LOC

To predict the result of a copper/graphene lab on chip, two approaches are possible. The first, simplistic approach, is to consider the stress test of a specimen composed of the superposition of two materials with different mechanical properties. The second considers not only the superposition but also the chemical and mechanical interactions between the two layers.

According to the first approach, copper should be reinforced by the presence of graphene. When actuated, both materials will be subjected to the same strain, and both copper and graphene will present an internal stress. One can thus expect that a copper/graphene specimen will deform less than only copper. This is checked theoretically by establishing the force balance of a released test structure with and without the graphene sheet, and by computing the displacement u that will be reached at equilibrium. The left part of the equation is the force of the actuator, which should be equal to the sum of the force in the copper layer and in the graphene sheet.

$$S_a E_a \left(ln\left(\frac{L_{a0}-u}{L_{a0}}\right) - \epsilon^a_{mis} \right) = S_{s,cu} E_{s,cu} \left(ln\left(\frac{L_{s0}+u}{L_{s0}}\right) - \epsilon^{s,cu}_{mis} \right) + S_{s,gr} E_{s,gr} ln\left(\frac{L_{s0}+u}{L_{s0}}\right) \tag{44}$$

where:

- S_a, $S_{s,cu}$ and $S_{s,gr}$ are the cross-sectional area of the nickel actuator, of copper and of graphene, respectively. For the example, one chooses a nickel actuator of 105 nm thick and 14 μm width. The specimen is 70 nm thick and 2.5 μm wide copper thin film, superposed or not by graphene with the same dimensions, and naturally about 0.3 nm thick.
- $E_a = 214\,GPa$[52; 53], $E_{s,cu} = 130\,GPa$ and $E_{s,gr} = 1000\,GPa$ [51] are the Young's moduli of nickel, copper and graphene, respectively.
- $\epsilon^a_{mis} = 0.004$ and $\epsilon^{s,cu}_{mis} = 0.0009$ are the mismatch of the nickel actuator and of the copper. There is no mismatch in the graphene sheet as it does not contain any internal stress.
- $L_{a0} = 1000\,\mu m$ and $L_{s0} = 100\,\mu m$ are the length of the actuator and specimen, respectively. Lastly, u is the displacement that should be determined to balance the forces in the test structure.

Filling in the parameters and numerically solving for u gives in the absence of graphene, a displacement of 1623 nm and a force of 0.747 mN. In the presence of graphene, the computed displacement is 1592 nm and the force is 0.757 mN. As expected, the presence of graphene decreases the computed displacement, in this case by 31 nm. The presence of graphene should thus be visible in the

experimentally. Still, 31 nm is in the same order of magnitude as the errors made in the displacement measurements. This result has been obtained for an actuator of 1000 μm long. For shorter actuators, the difference will be less. For a 50 microns actuator, the difference is 1.4 nm. For a 1500 microns actuator, the difference is 41 nm.

The second approach takes into account the interactions between the two materials, in particular regarding the effect on dislocations. A dislocation is a linear defect, corresponding to a discontinuity in the matter arrangement. Plastic deformation happens when many dislocations are created, displace and are multiplied. A material in which less or no dislocations can originate or displace will be less ductile. As dislocation sources and movements are highly constrained by grain boundaries, materials with small grain size (nanometer scale grains) will be able to reach higher stresses, because their grain boundary density is higher than for coarse-grained materials [57]. Bahrami *et al.*[58] showed in 2021 that the presence of graphene on a copper layer influences the movement of dislocations. This was done by comparing the nanoindentations on a thin copper film and on a thin film copper with an as grown graphene sheet. The result is that the presence of graphene prevents dislocations created inside the thin film by the indentation tip to escape from the surface. The high strength of graphene allows high stresses to build up at the edges of the copper film without failure, where graphene acts like a strong grain boundary. If dislocations cannot escape from the copper layer, they will be accumulated under the indent and their concentration will increase. The result is that an immobile network of dislocations appears, preventing new dislocations to displace freely in the film [59]. Graphene could thus be at the origin of strain hardening inside the copper thin film by saturating it with a motionless dislocation network. To make the dislocations escape through the graphene layer, the stress should be increased. These considerations suggest that graphene could significantly impact the relaxation rate of copper thin films.

4.6 Results for Copper+Graphene LOC

The measured copper/graphene sample is from the same wafer as the copper sample treated in Subsection 4.4. Therefore, all parameters should be the same (mismatch of copper, mismatch of nickel, as well as thicknesses and widths). Several free beams structures were measured on the copper/graphene sample. This allowed to compute a mismatch strain of 0.0040 for the nickel actuator and 0.0009 for the copper specimen.

Figure 57 shows in bluish colors the evolution of copper specimens one week after release and three weeks after release. In reddish colors, the evolution of copper/graphene samples over the same time intervals is depicted. Lack of measureable data makes that it was not possible to measure exactly the same structures on both samples. The structures of 2.5 μm width have the most comparable data points.

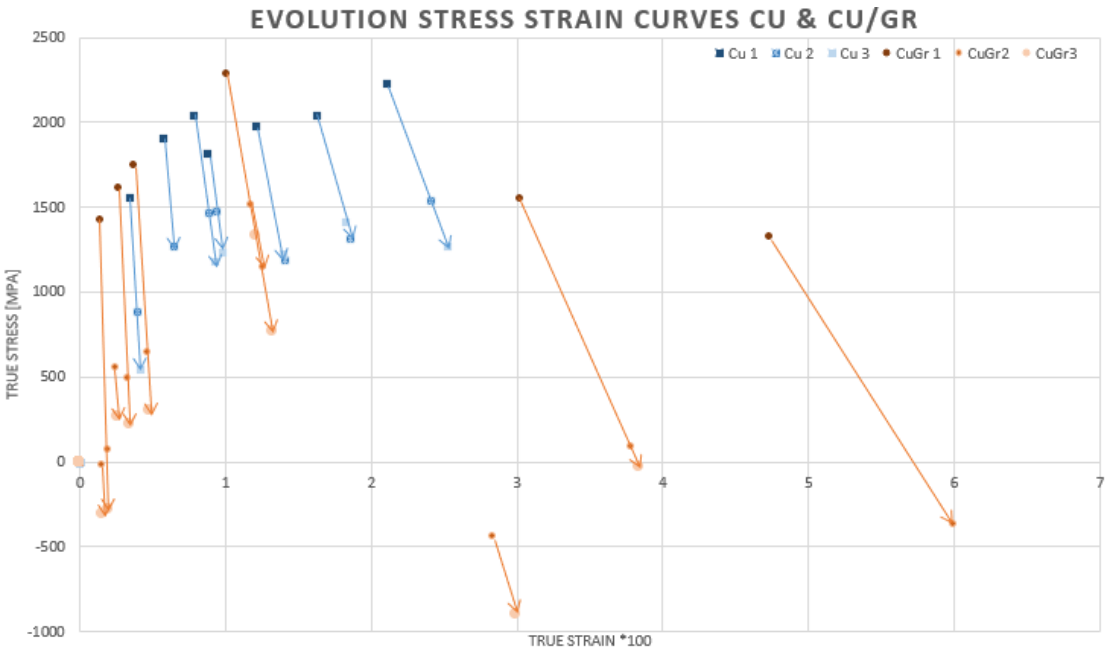

Figure 57: Comparison of the time-evolution's of stress strain curves of copper (bluish colors) and of copper/graphene specimen (reddish colors)

One observe that the evolution of the stress-strain state of the data points is the highest in the presence of graphene (the reddish lines are on average longer than the bluish lines). This was not expected in previous subsection. The reason of that unexpected graphene/copper behaviour is probably the adhesion between copper and graphene that is less than when graphene is grown on the copper thin film. The effect of graphene as a barrier for dislocations is probably not present.

The maximum true strain obtained for copper/graphene sample is around 0.06 (structure n°20 of 2.5 μm width an 50 μm length). This is slightly higher than the maximum true strain obtained for copper specimen (structure n°25 of 4 μm width an 50 μm length). As this result comes from one isolated measure and are from different test-structures width, it would be too fast to conclude that the higher strain is thanks to graphene.

One notes that the stresses reached in copper/graphene samples looks smaller in average. This can be due to premature rupture of the test-structures between the actuator and the specimen, because of the bad adhesion between copper and graphene.

5 Conclusion

The aim of this work was to quantify the influence of graphene on the mechanical properties of copper. For this purpose, a copper/graphene LOC process was developed, with the aim of comparing its results with those of copper LOC and graphene LOC.

LOC Graphene

For the process part, it has not been possible to reproduce graphene LOCs of the same quality as in August recently due to manufacturing problems. A sample from August was further released and measured to conclude that:

- The assumption that pulling on graphene specimens is like pulling on nothing at all is not valid. Graphene has an influence on the measured displacement.
- The measurement of self-actuated structures is not a good method to characterize the elastic mismatch of nickel, as these structures operate partially in the plastic regime.
- The properties of nickel need to be better known before it can be used as an actuator. In particular, its stress-strain curve is unknown and it is suspected that nickel behaves plastically for small deformations. Its plastic regime is probably reached during actuation, whereas an elastic behaviour was assumed.
- The behaviour of nickel evolves slightly with time, making the interpretation of the results even more complicated.

LOC Copper

The manufacturing process of the copper specimens is the same as that of copper/graphene, since they come from the graphene-free parts of copper/graphene wafers. From the copper specimens it was shown that:

- The calculation of the mismatch is crucial to get realistic orders of magnitude for the stress and Young's modulus. Free beam measurement is the most accurate method to use when nickel is used as an actuator.
- The time evolution of the same measurements was observed by re-measuring the structures one and three weeks after the first measurement. As expected, an evolution is observed, due to relaxation in copper and a reverse creep in nickel. This evolution slows down with time.

LOC Copper/Graphene

The manufacturing process of the copper/graphene samples was developed. However, there are still things to improve in order to be able to measure more structures: the lift-off problem and the copper-graphene adhesion problem. The time evolution of copper structures and copper-graphene structures were compared. It was expected that graphene would strengthen the copper, acting as a strong grain boundary on its surface, requiring greater stress to overcome. The experiment is contrary to this, as the stress-strain curve for copper/graphene has evolved more than that for copper. This is due to the imperfect adhesion of graphene on copper, and to the complexity of the process which makes that many structures are not measurable.

A Process LOC Graphene

Process sheet graphene LOC

Step	Name	What	Duration	Power	Amount	Waiting time before next step
1. Standard cleaning	bath 1	Pyranah	10 min			
	rinsing	water with N2 gas	10 min			
	bath 2	pyranah	10 min			
	rinsing	water with N2 gas	10 min			
	bath 3	HF 2%	15 sec			
	rinsing	water with N2 gas	5 min			
	bath 4	water with N2 gas	10 min			
	drying centrifuge	drying centrifuge		2000RPM		
2. Coating of photoresist	LPIII	Improving the adhesion of resist				as fast as possible
for alligmment marks	Spin coating	Negative resist spin coating		3000RPM		
	baking	Baking of the wafer in the oven	60 sec	90°C		
3. Patterning	Exposure	Exposure for first photolithography, vacuum contact		120ml/cm^2		
	PEB	Post exposure bake (LO Resist)	60 sec	105°C		
	Developpement		60 sec			
4. Ni deposition	Vacotec	Ni deposition/LIFT OFF mode			70nm	
5. Lift-Off nickel	Removing nickel	Acetone	30 min	70°C		
	Rinsing	Propanol, water				
6. Grahene transfer	PMMA coating	7% PMMA coating of the graphene foil		6000RPM	500nm	15 min
	Cu foil removal	Remove the underlaying copper foil in FeCl3	10 min			4-5 hours
	Gr transfer	Transfer the graphene on the Si with 'fishing' method				1 day in N2 environment
7. Removing PMMA	PMMA coating	2% PMMA coating of the whole wafer		6000RPM	100nm	
	Removal PMMA	Acetone	30 min	70°C		
	rinsing	Propanol, water				1 day in N2 environment
8. Coating of photoresist	LPIII	Improving the adhesion of resist				as fast as possible
for graphiene paterning	PMMA coating	2% PMMA coating of the whole wafer		6000RPM	100nm	15 min
	Spin coating	Azmir, positive resist spin coating		4000RPM		
	baking	Baking of the wafer in the oven	90 sec	90°C		
9. Patterning	Exposure	Exposure for first photolithography, vacuum contact		160ml/cm^2		
	PEB	Post exposure bake	90 sec	110°C		
	Developpement		60 sec			
10. Removing graphene	Oxygen plasma	Remove the graphene where no resist is protecting	1 min 30	40 W		
11. Removing Photoresist	Removal photoresist	Acetone	30 min	70°C		
	Rinsing	Propanol, water				
12. Coating of	LPIII	Improving the adhesion of resist				
photoresist	Spin coating	Negative resist spin coating		3000RPM		
for Ni deposition	baking	Baking of the wafer in the oven	60 sec	90°C		
13. Patterning	Exposure	Exposure for second photolithography, hard contact		120ml/cm^2		
	PEB	Post exposure bake (LO Resist)	90 sec	105°C		
	Developpement					
14. Ni deposition	Vacotec	Ni deposition/LIFT OFF mode			100-150nm	
15. Lift-Off nickel	Removing nickel	Acetone	30 min	70°C		
	Rinsing	Propanol, water				
16. Release	Release	Dry etching of the silicon under the samples with XeF2	10 sec	300Pa	~15 pulses	

B Process LOC Copper+Graphene

Process sheet copper/graphene LOC

Step	Name	What	Duration	Power	Amoun	Waiting time before next step
1. Standard cleaning	bath 1	pyranah	10 min			
	rinsing	water with N2 bubbles	10 min			
	bath 2	pyranah	10 min			
	rinsing	water with N2 bubbles	10 min			
	bath 3	HF 2%	15 sec			
	rinsing	water with N2 bubbles in portable bath	5 min			
	bath 4	water with N2 bubbles	10 min			
	drying centrifuge	drying centrifuge		2000RPM		as fast as possible
2. Cu deposition	Vacotec	Cu deposition/rotation mode			70nm	
3. Grahene transfer	PMMA coating	7% PMMA coating of the graphene foil		6000RPM	500nm	15 min
	Cu foil removal	remove the underlaying copper foil in FeCl3	10 min			4-5 hours in water
	Gr paper transfer	Transfer the graphene on the Cu thin film with paper				1 day in N2 environment
4. Removing PMMA	Removal PMMA	Acetone	30 min	70°C		
	rinsing	Propanol, water				1 day in N2 environment
5. Coating of photoresist	LPIII	Improving the adhesion of resist				as fast as possible
	Spin coating	Azmir 701, positive resist spin coating		3000RPM		
	baking	Baking of the wafer in the oven	90 sec	90°C		
6. Patterning	Exposure	Exposure for first photolithography, vacuum contact		125mJ/cm^2		
	PEB	Post exposure bake	90 sec	110°C		
	Developpement					
7. Removing graphene	Oxygen plasma	Remove the graphene where no resist is protecting	7 min	100 W		
8. Etching copper	Wet etching	APS	25 sec			
9. Removing Photoresist	Removal photoresis	Acetone	30 min	70°C		
	Rinsing	Propanol, water				4 hours in N2 environment
10. Coating of photoresist	LPIII	Improving the adhesion of resist				
	Spin coating	Negative resist spin coating		3000RPM		
	baking	Baking of the wafer in the oven	60 sec	90°C		
11. Patterning	Exposure	Exposure for second photolithography, hard contact		130mJ/cm^2		
	PEB	Post exposure bake	90 sec	110°C		
	Developpement					
12. Ni deposition	Vacotec	Ni deposition/LIFT OFF mode			90nm	
13. Lift-Off nickel	Removing nickel	Acetone	30 min	70°C		
	Rinsing	Propanol, water				4 hours in vacuum of XeF2
14. Release	Release	Dry etching of the silicon under the samples with XeF2	10 sec	400Pa	7 pulses	

References

[1] M. Yi and Z. Shen, "A review on mechanical exfoliation for the scalable production of graphene," *Journal of Materials Chemistry A*, vol. 3, no. 22, p. 11700–11715, 2015.

[2] B. Wu, D. Geng, Z. Xu, Y. Guo, L. Huang, Y. Xue, J. Chen, G. Yu, and Y. Liu, "Self-organized graphene crystal patterns," *NPG Asia Materials*, vol. 5, p. e36–e36, Feb 2013.

[3] R. A. Tarefder and H. Faisal, "Effects of dwell time and loading rate on the nanoindentation behavior of asphaltic materials," *Journal of Nanomechanics and Micromechanics*, vol. 3, p. 17–23, Jun 2013.

[4] M. F. Doerner and W. D. Nix, "A method for interpreting the data from depth-sensing indentation instruments," *Journal of Materials Research*, vol. 1, p. 601–609, Jul 1986.

[5] N. Cheung, "Micro-electro-mechanical systems (mems) fabrication," 2010.

[6] J. Florando, H. Fujimoto, Q. Ma, O. Kraft, R. Schwaiger, and W. D. Nix, "Measurement of thin film mechanical properties by microbeam bending," *MRS Proceedings*, vol. 563, p. 231, 1999.

[7] Y. Xiang, X. Chen, and J. Vlassak, "Plane-strain bulge test for thin films," *Journal of Materials Research*, vol. 20, no. 9, p. 2360–2370, 2005.

[8] W. Sharpe, B. Yuan, and R. Edwards, "A new technique for measuring the mechanical properties of thin films," *Journal of Microelectromechanical Systems*, vol. 6, p. 193–199, Sep 1997.

[9] T. Tsuchiya, O. Tabata, J. Sakata, and Y. Taga, "Specimen size effect on tensile strength of surface-micromachined polycrystalline silicon thin films," *Journal of Microelectromechanical Systems*, vol. 7, p. 106–113, Mar 1998.

[10] D. T. Read, Y.-W. Cheng, R. R. Keller, and J. D. McColskey, "Tensile properties of free-standing aluminum thin films," vol. 45, p. 583–589, Sep 2001.

[11] M. Haque and M. Saif, "Application of mems force sensors for in situ mechanical characterization of nano-scale thin films in sem and tem," *Sensors and Actuators A: Physical*, vol. 97–98, p. 239–245, Apr 2002.

[12] H. Espinosa, B. Prorok, and M. Fischer, "A methodology for determining mechanical properties of freestanding thin films and mems materials," *Journal of the Mechanics and Physics of Solids*, vol. 51, p. 47–67, Jan 2003.

[13] H. D. Espinosa, Y. Zhu, and N. Moldovan, "Design and operation of a mems-based material testing system for nanomechanical characterization," *Journal of Microelectromechanical Systems*, vol. 16, p. 1219–1231, Oct 2007.

[14] D. Kiener, W. Grosinger, G. Dehm, and R. Pippan, "A further step towards an understanding of size-dependent crystal plasticity: In situ tension experiments of miniaturized single-crystal copper samples," *Acta Materialia*, vol. 56, p. 580–592, Feb 2008.

[15] H. Guo, K. Chen, Y. Oh, K. Wang, C. Dejoie, S. A. Syed Asif, O. L. Warren, Z. W. Shan, J. Wu, and A. M. Minor, "Mechanics and dynamics of the strain-induced m1–m2 structural phase transition in individual vo2 nanowires," *Nano Letters*, vol. 11, p. 3207–3213, Aug 2011.

[16] C. D. M. Optics, "E-beam evaporation explained | cdm optics."

[17] Feb 2021. Page Version ID: 179547074.

[18] D. Hardwick, "The mechanical properties of thin films: A review," *Thin Solid Films*, vol. 154, p. 109–124, Nov 1987.

[19] W. A. de Heer, C. Berger, X. Wu, M. Sprinkle, Y. Hu, M. Ruan, J. A. Stroscio, P. N. First, R. Haddon, B. Piot, and et al., "Epitaxial graphene electronic structure and transport," *Journal of Physics D: Applied Physics*, vol. 43, p. 374007, Sep 2010.

[20] Z. Yan, Z. Peng, and J. M. Tour, "Chemical vapor deposition of graphene single crystals," *Accounts of Chemical Research*, vol. 47, p. 1327–1337, Apr 2014.

[21] B. Huet and J.-P. Raskin, "Pressure-controlled chemical vapor deposition of single-layer graphene with millimeter-size domains on thin copper film," *Chemistry of Materials*, vol. 29, p. 3431–3440, Apr 2017.

[22] B. Huet and J.-P. Raskin, "Role of cu foil in-situ annealing in controlling the size and thickness of cvd graphene domains," *Carbon*, vol. 129, p. 270–280, Apr 2018.

[23] B. Huet, X. Zhang, J. M. Redwing, D. W. Snyder, and J.-P. Raskin, "Multi-wafer batch synthesis of graphene on cu films by quasi-static flow chemical vapor deposition," *2D Materials*, vol. 6, p. 045032, Aug 2019.

[24] W. Oliver and G. Pharr, "An improved technique for determining hardness and elastic modulus using load and displacement sensing indentation experiments," *Journal of Materials Research*, vol. 7, p. 1564–1583, Jun 1992.

[25] M. Coulombier, *Nanomechanical lab on-chip for testing thin film materials and application to Al and Al(Si)*. PhD thesis, Université catholique de Louvain, Mar 2012.

[26] *Proceedings of the Royal Society of London. Series A, Containing Papers of a Mathematical and Physical Character*, vol. 82, p. 172–175, May 1909.

[27] M. Hammad, *Contributions to experimental mechanics of graphene*. PhD thesis, Université Catholique de Louvain, 2017.

[28] X. Chen, B. L. Kirsch, R. Senter, S. H. Tolbert, and V. Gupta, "Tensile testing of thin films supported on compliant substrates," *Mechanics of Materials*, vol. 41, p. 839–848, Jul 2009.

[29] T. P. Weihs, S. Hong, J. C. Bravman, and W. D. Nix, "Measuring the strength and stiffness of thin film materials by mechanically deflecting cantilever microbeams," *MRS Proceedings*, vol. 130, p. 87, 1988.

[30] J. Vlassak and W. Nix, "A new bulge test technique for the determination of young's modulus and poisson's ratio of thin films," *Journal of Materials Research*, vol. 7, p. 3242–3249, Dec 1992.

[31] J. S. Mitchell, C. A. Zorman, T. Kicher, S. Roy, and M. Mehregany, "Examination of bulge test for determining residual stress, young's modulus, and poisson's ratio of 3c-sic thin films," *Journal of Aerospace Engineering*, vol. 16, p. 46–54, Apr 2003.

[32] J. Y. Pan, P. Lin, F. Maseeh, and S. D. Senturia, "Verification of fem analysis of load-deflection methods for measuring mechanical properties of thin films," in *IEEE 4th Technical Digest on Solid-State Sensor and Actuator Workshop*, p. 70–73, Jun 1990.

[33] D. Maier-Schneider, J. Maibach, and E. Obermeier, "A new analytical solution for the load-deflection of square membranes," *Journal of Microelectromechanical Systems*, vol. 4, p. 238–241, Dec 1995.

[34] D. T. Read, Y.-W. Cheng, R. R. Keller, and J. D. McColskey, "Tensile properties of free-standing aluminum thin films," vol. 45, Sep 2001.

[35] C. Chisholm, H. Bei, M. Lowry, J. Oh, S. Syed Asif, O. Warren, Z. Shan, E. George, and A. Minor, "Dislocation starvation and exhaustion hardening in mo alloy nanofibers," *Acta Materialia*, vol. 60, p. 2258–2264, Mar 2012.

[36] A. Kundu, A. Bateman, B. Jaques, I. Charit, and C. Jiang, "A preliminary study on helium and sulfur ion-irradiated bcc iron: In situ tensile testing using a push-to-pull device," *JOM*, vol. 72, p. 2398–2407, Jun 2020.

[37] N. R. Velez, F. I. Allen, M. A. Jones, J. Donohue, W. Li, K. Pister, S. Govindjee, G. F. Meyers, and A. M. Minor, "Nanomechanical testing of freestanding polymer films: in situ tensile testing and tg measurement," *Journal of Materials Research*, Apr 2021.

[38] P. V. Kiryukhantsev-Korneev, P. A. Loginov, A. S. Orekhov, and E. A. Levashov, "Study of nanomechanical properties of thin films using in-situ "push-to-pull" method in the column of transmission electron microscope," *Journal of Physics: Conference Series*, vol. 1688, p. 012004, Nov 2020.

[39] S. Gravier, M. Coulombier, A. Safi, N. Andre, A. Boe, J.-P. Raskin, and T. Pardoen, "New on-chip nanomechanical testing laboratory - applications to aluminum and polysilicon thin films," *Journal of Microelectromechanical Systems*, vol. 18, p. 555–569, Jun 2009.

[40] Apr 2021. Page Version ID: 1016254988.

[41] A. Baptista, F. Silva, J. Porteiro, J. Míguez, and G. Pinto, "Sputtering physical vapour deposition (pvd) coatings: A critical review on process improvement and market trend demands," *Coatings*, vol. 8, p. 402, Nov 2018.

[42] *Xetch® e1 Series™ Bulk Silicon Etch System Users Manual*.

[43] H. F. Winters and J. W. Coburn, "The etching of silicon with xef2 vapor," *Applied Physics Letters*, vol. 34, p. 70–73, Jan 1979.

[44] M. Gaudet, *Conception, réalisation et caractérisation des microcanaux pour les applications microfluidiques*. PhD thesis, Université des sciences et technologies de Lille, 2006.

[45] Z. Cao, P. Wang, W. Gao, L. Tao, J. Suk, R. Ruoff, D. Akinwande, R. Huang, and K. Liechti, "A blister test for interfacial adhesion of large-scale transferred graphene," *Carbon*, vol. 69, p. 390–400, Apr 2014.

[46] K. Davami, Y. Jiang, C. Lin, J. Cortes, J. T. Robinson, K. T. Turner, and I. Bargatin, "Modification of mechanical properties of vertical graphene sheets via fluorination," *RSC Advances*, vol. 6, no. 14, p. 11161–11166, 2016.

[47] J. T. Robinson, J. S. Burgess, C. E. Junkermeier, S. C. Badescu, T. L. Reinecke, F. K. Perkins, M. K. Zalalutdniov, J. W. Baldwin, J. C. Culbertson, P. E. Sheehan, and et al., "Properties of fluorinated graphene films," *Nano Letters*, vol. 10, p. 3001–3005, Aug 2010.

[48] R. Stine, W.-K. Lee, K. E. Whitener, J. T. Robinson, and P. E. Sheehan, "Chemical stability of graphene fluoride produced by exposure to xef 2," *Nano Letters*, vol. 13, p. 4311–4316, Sep 2013.

[49] S. J. Hearne, *Origins of Stress During Electrodeposition.* No. SAND2008-2533C, Apr 2008.

[50] M. Ghidelli, H. Idrissi, S. Gravier, J.-J. Blandin, J.-P. Raskin, D. Schryvers, and T. Pardoen, "Homogeneous flow and size dependent mechanical behavior in highly ductile zr65ni35 metallic glass films," *Acta Materialia*, vol. 131, p. 246–259, Jun 2017.

[51] S. Thomas, K. M. Ajith, S. U. Lee, and M. C. Valsakumar, "Assessment of the mechanical properties of monolayer graphene using the energy and strain-fluctuation methods," *RSC Advances*, vol. 8, no. 48, p. 27283–27292, 2018.

[52] D. C. Baek, T. S. Park, and S. B. Lee, "Measurement of mechanical properties of electroplated nickel thin film," *Key Engineering Materials*, vol. 261–263, p. 417–422, Apr 2004.

[53] J. Luo, "Young's modulus of electroplated ni thin film for mems applications," *Materials Letters*, vol. 58, p. 2306–2309, Jul 2004.

[54] L. Delannay, G. Lemoine, M. Coulombier, and T. Pardoen, "Modelling creep induced by internal stresses in freestanding submicron cu film," *IOP Conference Series: Materials Science and Engineering*, vol. 580, p. 012003, Dec 2019.

[55] A. Haseeb, "Modeling of the effects of athermal flow strength and activation energy for dislocation glide on the nanoindentation creep of nickel thin film at room temperature," *Computational Materials Science*, vol. 37, p. 278–283, Sep 2006.

[56] A. Boé, A. Safi, M. Coulombier, T. Pardoen, and J.-P. Raskin, "Internal stress relaxation based method for elastic stiffness characterization of very thin films," *Thin Solid Films*, vol. 518, p. 260–264, Nov 2009.

[57] N. Ghazi and J. W. Kysar, "Experimental investigation of plastic strain recovery and creep in nanocrystalline copper thin films," *Experimental Mechanics*, vol. 56, p. 1351–1362, Oct 2016.

[58] F. Bahrami, M. Hammad, M. Fivel, B. Huet, C. D'Haese, L. Ding, B. Nysten, H. Idrissi, J. Raskin, and T. Pardoen, "Single layer graphene controlled surface and bulk indentation plasticity in copper," *International Journal of Plasticity*, vol. 138, p. 102936, Mar 2021.

[59] Z. Budrovic, "Plastic deformation with reversible peak broadening in nanocrystalline nickel," *Science*, vol. 304, p. 273–276, Apr 2004.

UNIVERSITÉ CATHOLIQUE DE LOUVAIN
École polytechnique de Louvain
Rue Archimède, 1 bte L6.11.01, 1348 Louvain-la-Neuve, Belgique | **www.uclouvain.be/epl**